It is not true that people stop pursuing dreams because they grow old, they grow old because they stop pursuing dreams.
Gabriel García Márquez

To my wife, Monica.

Jesús D. Gómez
New Mexico Institute of Mining and Technology
May, 2008

SENSIBLE AND LATENT HEAT FLUX ESTIMATION USING OPTICAL SCINTILLOMETRY

by

Jesús D. Gómez

Submitted in Partial Fulfillment
of the Requirements for the Degree of
Master of Science in Hydrology

New Mexico Institute of Mining and Technology
Socorro, New Mexico
May, 2008

ABSTRACT

The estimation of spatial and temporal distributions of sensible (H) and latent (λET) heat fluxes is a long standing challenge for hydrologic science. In this study, we present our experiences with the emerging method of scintillometry. Large Aperture Scintillometers (LAS) operating at optical wavelengths are employed to measure the sensible heat flux over irrigated fields, riparian areas, deserts, lava flows, and mountain highlands in New Mexico. The LAS transects were used to explore this measurement technique as a potentially useful tool in hydrological applications.

The main theoretical and technical aspects of the setup, operation, and analysis of LAS data are discussed. The advantages of a larger footprint, compared with other standard techniques used for the measurement of H, are explained, particularly in the context of the calibration and validation of remote sensing algorithms used for the estimation of turbulent fluxes, and hydrologic and meteorological models. Although, the measured data was not compared with remote sensing data, some of the main issues of this comparison are addressed and will be the objective of future research. Finally, scintilllometer data were used for the estimation of sensible (averages over 10-min and daily time intervals) and latent (averages over daily time intervals) heat fluxes. λET

was estimated as the residual of the surface energy balance (SEB), assuming closure, as a example of the estimation of evapotranspiration rates for hydrologic applications at scales of the pixel-size of satellite images or grid cells of hydrologic and meteorological models ($\sim$0.1-10 km^2).

ACKNOWLEDGMENT

The author wishes to thank Jan Hendrickx, who supervised this work, and the committee members for this research, Jan Kleissl, Enrique Vivoni, and Hector Erives for helpful discussion and their constructive comments. Finally, the author is indebted to Oscar K. Hartogensis, Ricardo Mantilla, George Diak, and Jaron Andrews for their disinterested help during this academic journey.

The following sponsors have contributed to this study: NSF EPSCoR grant EPS-0447691; U.S. Department of Agriculture, CSREES grant No.: 2003-35102-13654; NASA Cooperative Agreement NNA06CN01A; and the NSF Science and Technology Center program Sustainability of Semi-Arid Hydrology and Riparian Areas (SAHRA; EAR-9876800). Funding for three scintillometers for the Panama/Colombia network has been granted by ARO/DURIP grant52085-EV-RIP.

This report was typeset with LaTeX[1] by the author.

[1] LaTeX document preparation system was developed by Leslie Lamport as a special version of Donald Knuth's TeX program for computer typesetting. TeX is a trademark of the American Mathematical Society. The LaTeX macro package for the New Mexico Institute of Mining and Technology report format was adapted from Gerald Arnold's modification of the LaTeX macro package for The University of Texas at Austin by Khe-Sing The.

TABLE OF CONTENTS

LIST OF TABLES **iv**

LIST OF FIGURES **v**

1. INTRODUCTION **1**

2. SCINTILLOMETRY **6**

2.1 Theory 6

2.1.1 Derivation of the Sensible Heat Flux 7

2.2 Instrumentation 14

3. MATERIALS AND METHODS **20**

3.1 New Mexico Scintillometer Network (NM-LASNet) 20

3.2 Intercomparison Experiment Set-up 22

3.3 Saturation Experiment Set-up 27

4. SCINTILLOMETER MEASUREMENTS AND DATA ANALYSIS **30**

4.1 Instrument Set-up and Operation 30

4.2 Stable and Unstable Atmospheric Conditions 32

4.3 The Effective Beam Height 35

4.4 Saturation 37

4.5 The Footprint 38

4.5.1 Footprint for Scintillometer Measurements 44
4.5.2 Limitations of Footprint Models and its Use for Validation and Calibration of Remote Sensing Algorithms . . . 51
4.6 Effects of High Wind Speeds and Tower Vibrations 53
4.7 Effects of Misalignment 54

5. APPLICATIONS **57**
5.1 Estimation of Sensible Heat Fluxes from LAS 57
5.2 Estimation of Evapotranspiration from LAS and the Energy Balance 61

6. GENERAL CONCLUSIONS AND LESSONS LEARNED **70**

A. LIST OF SYMBOLS **76**

Bibliography **78**

LIST OF TABLES

3.1 NM-LASNet. All locations are given in UTM 13 (WGS 84), unless otherwise noted. z_o: roughness length, d: zero displacement height. Meteorological sensors: R_{sd}: shortwave downwelling radiation, $wspd$: wind speed, $wdir$: wind direction, T: Temperature, RH: relative humidity, T_{sfc}: IR surface temperature, EC/EB: Eddy covariance/Energy balance, soil: soil temperature, moisture, conductivity at 0.1 m. 23

3.2 Instrumentation for the intercomparison experiment. 28

LIST OF FIGURES

2.1 Layout of scintillometer system and integration of refractances of turbulent structures (Wageningen Agricultural University, 2002). 7

2.2 LAS normalized weighting function, $G(x')$, along the normalized path x'. 10

2.3 Correction to C_T^2 by humidity fluctuations in different climates. (a) Tropical rain forest, where high annual rainfall keeps soils wet year-round (1.97 -5.74%), (b) temperate forest and grasslands, where less rainfall causes drier soils (0.75-1.48 %), (c) semi-arid regions with dry soils (0.10-0.30 %), and (d) deserts (less than 0.06 %). Typical Bowen ratios for each climate where taken from Bonan (2002). 13

3.1 Locations of LAS transects in New Mexico (the transect consist of transmitter and receiver). The surface albedo map was generated with SEBAL in June 16 of 2002. 22

3.2 LAS setup locations in New Mexico: San Acacia alfalfa crop (SAA), San Acacia riparian area (SAR), El Malpais basalt outcrops (EMNM), Sevilleta National Wildlife Refuge (SNWR), and Valles Caldera mountainous grassland (VCNP). 24

3.3 Topographic characteristics of LAS transects in New Mexico. Scintillometer beam elevation Z_{beam} (gray line), surface elevation Z_{sfc} (black line). The scintillometer beam height, along the path x, can be estimated as $Z_{LAS}(x) = Z_{beam} - Z_{sfc}$. 25

3.4 Sketch of the saturation set-up. T stands for transmitter and R for receiver. 29

4.1 Example of diurnal cycle of C_n^2 obtained with a LAS for a sunny day at the Sevilleta National Wildlife Refuge LAS transect on February 3, 2006. Note the steep drop in C_n^2 when atmospheric stability changes from stable to unstable and back to stable. . . 34

4.2 Comparison of C_n^2 for a LAS and XLAS during the saturation experiment at Sevilleta National Wildlife Refuge (July 14-17, 2007). The C_n^2 (LAS) levels off at large C_n^2 indicating saturation. 39

4.3 Example of a one-dimensional footprint with the HKC-model (left) and the lateral dispersion in the cross-wind direction (right). Assuming a normal distribution (see Eq. (**??**)), 99.8% of the lateral fluxes are between $3\sigma_y$. 44

4.4 Footprint function [m^{-1}] at the VCNP site on May 1, 2007 1400h MST for: (a) LAS with wind direction parallel to the transect (95% of the footprint function is represented by an area of 1.3 km^2), (b) LAS with wind direction perpendicular to the transect (95% of the footprint function is represented by an area of 2.3 km^2), (c) fictitious EC at 3 m height with wind direction parallel to the transect (95% of the footprint function is represented by an area of 0.09 km^2), (d) fictitious EC at 3 m height with wind direction perpendicular to the transect (95% of the footprint function is represented by an area of 0.09 km^2). Parameters used are: $\overline{U} = 5.5ms^{-1}$, $\overline{\theta} = 17.5$ degrees, $\sigma_\theta = 15.6$ degrees, $z_0 = 0.02m$, and $L_{MO} = -20$. The LAS transect was discretized in 50 points. 46

4.5 Variability of the footprint function with respect to the wind direction (azimuth) for a LAS. The color scale is not included, but the footprint values vary from high (red) to low (blue). The white line corresponds to the LAS transect. For the simulations: $L = 2000$ m, $\sigma_v = 1$ m/s, $L_{MO} = -50$ m, and $Z_eff = 10$ m. . . 48

4.6 Variability of the footprint function with respect to the wind direction (azimuth) for a EC. The color scale is not included, but the footprint values vary from high (red) to low (blue). The white line corresponds to the LAS transect (Fig. **??**). For the simulations: $\sigma_v = 1$ m/s, $L_{MO} = -50$ m, and $Z = 10$ m. 49

4.7 Variability of the footprint function with respect to the wind direction (azimuth) for an EC (Fig. **??**) and LAS (Fig. **??**). The red dots correspond to the peaks of the footprint for the wind direction used in Figs. **??** and **??**. The black line corresponds to the LAS transect and the black circle to the EC. For the simulations: $\sigma_v = 1$ m/s, $L_{MO} = -50$ m, and $Z = 10$ m. 50

4.8 Top: Intercomparison of sensible heat flux measurements from four LASs (symbols), EC (purple line), and net radiation (black line) at the Sevilleta National Wildlife Refuge (SNWR) site (table 3.1) in December 7-8, 2005. Bottom: Wind speed at SNWR for the same days. 54

4.9 Top: Comparison of sensible heat fluxes estimated at SNWR during June-July of 2006 (EC black line and LAS red dots). Bottom: signal strength (demod) for the LAS. 56

4.10 Scatter plot of sensible heat fluxes measured with a LAS and an EC system at SNWR during June-July of 2006. 56

5.1 Periods with availability of sensible heat fluxes from the NM-LASNet. Three main time intervals were chosen for the diurnal cycle analysis: (i) Fall, (ii) Winter and (iii) Spring. 59

5.2 Daily sensible heat fluxes from the NM-LASNet. 60

5.3 Average diurnal cycles at: SAA (red line), SAR (blue line with triangles), EMNM (blue line with squares), SNWR (purple line with circles), and , VCNP (black line with triangles). From upper row to bottom: Mean daytime evolution (H), standard deviation (σ_H), coefficient of variation ($CV = \frac{\sigma_H}{\overline{H}}$), coefficient of variation during unstable atmospheric conditions ($CV = \frac{\sigma_H}{\overline{H}}$). The Spring period is 04/2407 - 05/14/07, Fall is 09/07/06 - 09/24/06 and Winter is 11/07/06 - 12/01/06. 62

5.4 Data used for ET estimation: SNWR (upper row) and VCNP (lower row). In the figures to the left: R_n (red dashed line), G (green line), H_{LAS} (black line), and H_{EC} (blue squares). In the figures to the right: scatter plots of the sensible heat fluxes estimated with LAS (x-axis) and EC (y-axis). 67

5.5 Daily latent heat flux for: (a)-(b) SNWR from January 20 to February 7 of 2006 and (c)-(d) VCNP from June 8 to June 25 of 2006 (lower row). In the figures to the left: R_n^{24} (red line with circles), H^{24} (black line with squares), G^{24} (green line with dots), and λET^{24} (blue line with triangles). 69

This report is accepted on behalf of the faculty of the Institute by the following committee:

Jan M.H. Hendrickx, Advisor

Jesús D. Gómez

Date

CHAPTER 1

INTRODUCTION

The estimation of the temporal and spatial variability of energy fluxes has important applications in agriculture, meteorology, hydrology, and water management. Particularly, in arid and semi-arid watersheds, evapotranspiration (ET) is one of the most critical variables for sustainable management of water resources (Middle Rio Grande Water Assembly, 1999), not only for the large percentage of the water budget that it represents, but also for its highly variable behavior at different spatial and temporal scales, and the uncertainty associated with its estimation (Goodrich et al., 2000).

During the last two decades, the feasibility of using optical remote sensing data for the estimation of the regional distributions of sensible and latent heat fluxes has been explored. As a result, several operational remote sensing algorithms were developed, such as $SEBAL$ (Surface Energy Balance Algorithms for Land, Bastiaanssen et al. (1998)), $METRIC^{TM}$ (Mapping ET at high spatial Resolution with Internalized Calibration, Allen et al. (2006)), ALEXI (Atmosphere-Land Exchange Inverse Model, (Anderson et al., 2004)), $DisALEXI$ (Disaggregated Atmosphere-Land Exchange Inverse Model, (Norman et al., 1995)), $NLDAS$ (North American Land Data Assimilation System) and LIS (Land Information System, (Peters Lidard et al., 2004)), among others.

These algorithms are different in their spatial and temporal scales (30 m to 1/8th degree which is about 13 km in New Mexico, daily to monthly), producing ET maps on local, regional, or national scales. However, the lack of ground-truth measurements at scales comparable to the algorithm resolution (30m for Landsat, 1000m for MODIS, and 4000m for GOES thermal IR pixels) represents a major difficulty for their calibration and validation. The algorithms estimate an areally-average sensible or latent heat flux for an area that: (i) is several orders of magnitude larger than the area represented by the most common measurement techniques for turbulent fluxes (Eddy Covariance or Bowen Ratio), and (ii) posses a high spatial variability of of turbulent fluxes. Therefore, the comparison of almost a point measurement, in a highly variable space, with an areally-average value, may lead to erroneous conclusions.

Currently, the most common measurement technique for turbulent fluxes is the eddy covariance method (EC) (e.g. Katul et al. (1999)). An EC system typically consists of a 3D sonic anemometer-thermometer (SAT) operated at 10 Hz or higher and a scalar sensor in close proximity (for sensible heat flux, a finewire thermocouple or virtual temperature from the sonic anemometer; and, for latent heat flux, a krypton hygrometer or infrared gas analyzer). The sensible heat flux H, and latent heat flux λET, are then computed directly from covariances of the vertical wind velocity w, air temperature T, and humidity q, as

$$H = \rho c_p \overline{w'T'} \tag{1.1}$$

$$\lambda ET = \rho \overline{w'q'} \tag{1.2}$$

where ρ is the air density, c_p is the specific heat capacity at constant pressure, the bar denotes temporal averaging, and w', T', and q' are the differences between, respectively, the instantaneous vertical wind speed, air temperature, specific humidity and their means over 10 to 30 minutes. This approach is based in the Reynolds decomposition of quantities into their mean and fluctuating parts. Mean values will be marked with an overbar, fluctuating contributions by a prime, e.g:

$$[u, v, w] = [(\overline{u} + u'), (\overline{v} + v'), (\overline{w} + w')] \tag{1.3}$$

$$T = \overline{T} + T' \tag{1.4}$$

$$q = \overline{q} + q' \tag{1.5}$$

However, several non-trivial corrections have to be applied to the measurements (Van Dijk et al., 2004), and even then the sum of the sensible and latent turbulent fluxes from EC systems are typically 10-30% smaller than available energy, i.e. the difference of net radiation (R_{net}) and soil heat flux (G), an issue known as energy balance closure which has yet to be resolved (e.g. Wilson et al. (2002); Culf et al. (2004)). Mahrt (1998) discussed several reasons for lack of closure of the surface energy budget: (i) lack of coincidence of the source areas among various flux components measured very near a surface such

as evaporation coming from leaves and sensible heat from a hot, dry soil surface; (ii) flux divergence arising from transport that is not one dimensional in the vertical such as insufficient fetch; (iii) non-stationarity of measured time series over the typical 30 min averaging periods so that covariance arising from very low frequency fluctuations is missed; (iv) turbulent dispersive fluxes arising from organized planetary-boundary-layer circulations that may have preferred locations so that the mean vertical velocities at an instrument location may be systematically different from zero giving rise to a vertical advective flux; and (v) measurement errors related to sensor separation, frequency response, alignment problems, and interference from tower or instrument-mounting structures.

In addition, the EC method only provides point measurements with a footprint scale that may be considerably smaller than the estimate obtained from a remote sensing method. On clear days with unstable atmospheric conditions the EC's footprint of H and λET is typically on the order of 10^{-1} km^2, while a MODIS or GOES image has an area on the order of 1 km^2. Therefore, it is highly affected by the spatial and temporal variability of the footprint which mostly depends on atmospheric stability and wind direction (e.g. Hsieh et al. (2000); Horst and Weil (1992); Schmid and Oke (1990)). To mitigate these issues, a dense network of stations is needed to obtain areally averaged fluxes (e.g. Meijninger et al. (2002)).

On the other hand, scintillometry, particularly the Large Aperture Scintillometer (LAS), has emerged as an alternative method to avoid several of the complications mentioned above (De Bruin, 2002). In hydrological applications, scintillometry has several advantages over EC, such as robustness,

because the proper operation can be verified in the field and relatively easy installation, maintainability, and data analysis. Since LAS is a remote sensor, instruments can be installed at the border of agriculture fields without disturbing the experimental site or interfering with agricultural operations. Moreover, the scintillometer footprint is better constrained, defined, and is large enough to allow the measurement of vertical sensible heat flux averaged over areas comparable with several pixels of a satellite image (up to about 40 Landsat thermal pixels or about 5 MODIS thermal pixels) (see Section 4.5 in this document or Hendrickx et al. (2007) for further explanation).

Meijninger (2003) presented a systematic study of the LAS performance over heterogeneous flat agricultural terrain in the Flevopolder (The Netherlands). The conclusion of this study is that LAS can accurately derive area-averaged sensible heat fluxes over heterogeneous areas. Also, previous studies have shown the potential of scintillometers as a tool for the estimation of latent heat fluxes in irrigated areas. Hoedjes et al. (2002) evaluated the potential of scintillometers over an irrigated wheat field in a semi-arid region in northwest Mexico, and Hartogensis and De Bruin (2006) used optical scintillometers for the estimation of fluxes at field-scale over agricultural areas in Idaho, obtaining promising results in both cases.

The aim of this thesis is to discuss the fundamentals and demonstrate the potential of LAS for hydrological applications, based on the experiences of a continuously operating network of large aperture scintillometers and some related experiments. Chapter 2 gives a description of the theory and instrumentation behind a LAS. Chapter 3 describes the experimental set-ups used

in this study. Chapter 4 reviews some important aspects of the scintillometer measurements and data analysis. Chapter 5 presents the LAS measurements of sensible heat fluxes at 10 minutes and daily scales as well as the daily estimates of latent heat fluxes as the residual of the energy balance equation. Chapter 6 gives some lessons learned and conclusions. Finally, the appendices contain a list of symbols used in the document.

CHAPTER 2

SCINTILLOMETRY

2.1 Theory

A large aperture scintillometer (LAS) is an instrument that consists of a transmitter and a receiver (Fig. 2.1). The receiver measures intensity fluctuations in the radiation emitted by the transmitter caused by refractive scattering due to turbulent eddies in the LAS path. For the LAS, the observed intensity fluctuations are a measure of the structure parameter of the refractive index of air, C_n^2. At optical wavelengths, the contribution of temperature fluctuations dominates, i.e., the structure parameter of temperature, C_T^2, can be deduced from C_n^2. For radio wavelengths (> 1 mm), on the other hand, water vapor fluctuations contribute most to the scintillometer signal fluctuation, i.e. the structure parameter of water vapor C_q^2 can be deduced from C_n^2. Using the Monin-Obukov similarity theory in the atmospheric surface layer, surface fluxes of sensible heat H, latent heat λET, and momentum can be determined from C_T^2, C_q^2, Bowen ratio ($Bo = H/\lambda ET$), and supplemental meteorological measurements such as wind speed and direction, air temperature, air pressure, roughness length.

It is important to note that in order to estimate H, a measure of the mechanically induced turbulence is needed since it contributes to the transport of sensible heat, but is not measured by the LAS. Flux profile relationships are

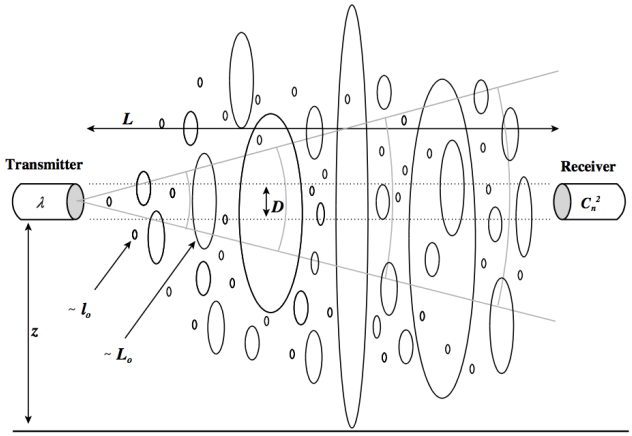

Figure 2.1: Layout of scintillometer system and integration of refractances of turbulent structures (Wageningen Agricultural University, 2002).

applied using wind speed measurement at one height and roughness length to estimate the friction velocity (u_*), which is related to the momentum transport. This limitation of LASs plays an important role in stable atmospheric conditions, where mechanically generated turbulence is the only turbulence generating transport mechanism (Hartogensis and De Bruin, 2006), leading to higher uncertainty in the estimated fluxes under this condition.

2.1.1 Derivation of the Sensible Heat Flux

To describe spatial variability of a variable in a random field, turbulence theory uses the structure parameter. For instance, let X be any variable (e.g. Temperature (T), Velocity (U), Specific humidity (q), or refraction index (n)) that undergo irregular random fluctuations in a turbulent atmosphere (random processes that vary in space and time). The structure parameter of X is defined as:

$$C_X^2 = \frac{\overline{(X(r_1) - X(r_2))^2}}{r_{1,2}^{2/3}} \tag{2.1}$$

where C_X^2 is the structure parameter of the variable X, $X(r_1)$ and $X(r_2)$ are the values at locations r_1 and r_2, respectively, and $r_{1,2} = |r_1 - r_2|$ is the distance between locations.

Eq. (2.1) assumes that the random field is statistically homogeneous (it has constant mean and C_X^2 is unaffected by a simultaneous translation of r_1 and r_2 in the same direction by the same amount) and isotropic (C_X^2 only depends on $r_{1,2}$ and not the direction), and X is mainly influenced by inhomogeneities in the random field, that are smaller than $r_{1,2}$. The distance $r_{1,2}$ lies in the inertial range of turbulence.

Taking into account the turbulent nature of the atmospheric boundary layer (ABL), it can be described by a wide range of three-dimensional whorls, usually called eddies. The largest eddies are caused by wind shear and convection and have sizes on the order of the boundary layer depth. These eddies are unstable and break down into smaller and smaller eddies (cascade process), introducing energy into the system until they reach the size L_0, called the outer scale of turbulence (it scales with a length and is on the order of half the height above the surface). For eddies smaller than L_0 only the inertial transfer of energy is important, until they reach the size l_0, called the inner scale of turbulence (approximately equal to 1 mm), in which the kinetic energy is dissipated into heat at the smallest molecular length scales. The energy spectrum of turbulence, relates the the distribution of kinetic energy (ϕ_n) with

the wave number ($k = 2\pi/l$), where l is the size of the eddies. Based in this definition, the inertial range is defined as the interval $[2\pi/L_0, 2\pi/l_0]$.

The statistics of propagation of electromagnetic (EM) radiation through the turbulent atmosphere allows the estimation of C_n^2. EM radiation propagating through the atmosphere is mainly affected by scattering, absorption, and fluctuations in the refractive index of air (n), the last being usually the most important in clear air. Those processes will change the main characteristics of the EM wave, such as intensity or amplitude, polarization, and phase. Wang et al. (1978) derived the following expression relating the variance of the logarithm of the intensity fluctuations for an electromagnetic wave propagating through the atmosphere, $\sigma^2_{\ln(I)}$, to C_n^2, under the assumption of weak-scattering conditions and for a statistically homogeneous and isotropic refractivity field:

$$\sigma^2_{\ln(I)} = \int_0^1 C_n^2(x')W(x')dx' \tag{2.2}$$

where $W(x')$ is a weighting function that describes the contribution of each point along the path to the total LAS signal. $W(x')$ is a bell-shaped function with maximum values toward the middle of the path and zero at the receiver and transmitter.

$$W(x') = 16\pi^2 K^2 L \int_0^\infty k dk \phi_n(k) \left(\frac{2J_1(x_1)2J_1(x_2)}{x_1 x_2} \right)^2 \sin^2 \left(\frac{k^2 L x'(1-x')}{2K} \right) dk \tag{2.3}$$

where $x' = x/L$ is the dimensionless coordinate along a propagation path of length L, $K = 2\pi/\lambda$ is the optical wavenumber, k is the spatial wave number,

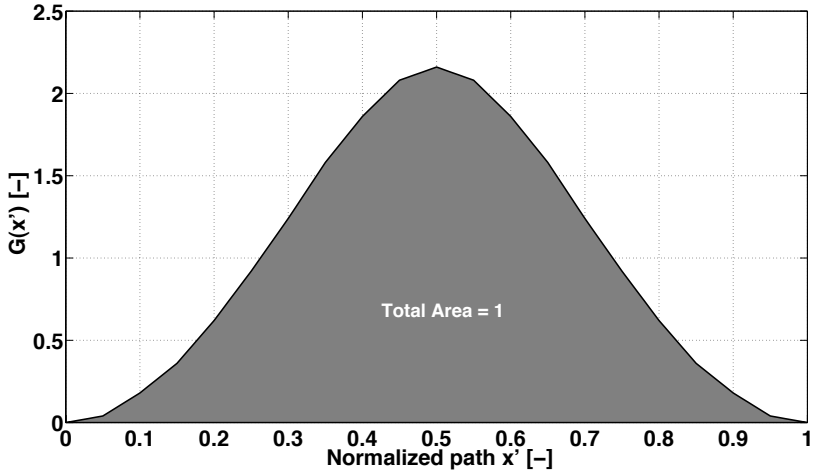

Figure 2.2: LAS normalized weighting function, $G(x')$, along the normalized path x'.

$\phi_n(k)$ is the three-dimensional spectrum of refractive index fluctuations for the atmosphere in the inertial range ($\phi_n(k) = 0.033C_n^2(x')k^{-11/3}$) (Kolmogorov, 1941), and $J_1(x_1)$ and $J_1(x_2)$ are Bessel functions of the first kind with $x_1 = kDx'/2$ and $x_2 = [kD(1-x')]/2$, where D is the aperture diameter.

Fig. 2.2 shows the normalized weighting function $G(x')$ ($G(x') = W(x')/\int_0^1 W(x')dx'$) for a LAS, evidencing the high sensibility of the LAS in the middle of the path.

The aperture diameter determines the sensitivity of a scintillometer to certain eddy sizes. For the Small Aperture Scintillometer (SAS), these eddies are in the order of the inner scale of turbulence (l_o). Then the exact form of $\phi(k)$ in the dissipation range of turbulence in the atmosphere is critical for the device performance. However, the large aperture scintillometer (LAS) is more sensitive to eddy sizes on the order of the aperture diameter (D), and therefore

less sensitive to $\phi(k)$.

Substituting equation Eq. (2.3) into Eq. (2.2) and integrating numerically, Wang et al. (1978) obtained the path-average for the structure parameter of the refraction index of air.

$$\overline{C_n^2} = 1.12\sigma^2_{\ln(I)} D^{7/3} L^{-3}. \tag{2.4}$$

C_n^2 can be expressed as a function of the structure parameters of temperature (C_T^2) and specific humidity (C_q^2), assuming a negligible effect due to pressure variations (i.e. C_p^2 is small compared to C_T^2 and C_q^2), as (Hill et al., 1980):

$$C_n^2 = \frac{A_T^2 C_T^2}{\overline{T^2}} + 2\frac{A_T A_q C_{Tq}}{\overline{Tq}} + \frac{A_q^2 C_q^2}{\overline{q^2}} \tag{2.5}$$

with

$$A_T = -0.78\frac{p}{T}10^{-6} \tag{2.6}$$

$$A_q = -57.22q10^{-6} \tag{2.7}$$

where p is the atmospheric pressure $[Pa]$, T is the temperature $[K]$, q is the specific humidity $[KgKg^{-1}]$, and C_{Tq} is the structure parameter for the covariant temperature and humidity fluctuations.

At the wavelength of the LAS ($\lambda_{LAS} = 0.88\mu m$), the contribution of C_q^2 to C_n^2 is much less important than the contribution of C_T^2. Therefore,

Eq. (2.5) can be rewritten into an expression for C_T^2, with a correction term depending on the Bowen ratio, Bo, to represent the contribution of C_q^2. Bo is equal to the ratio $H/\lambda ET$. Then, for a LAS (Hill, 1997)

$$C_T^2 = \left(\frac{C_{n_{LAS}}^2 \overline{T}^4}{A_{T_{LAS}}^2 \overline{p}^2} \right) \left(1 + \frac{0.03}{Bo} \right)^{-2}. \tag{2.8}$$

Therefore, the importance of the correction by humidity fluctuations depends on the meteorological conditions and surface properties, including soil moisture. Fig. 2.3 shows the percentage of the correction to C_T^2 when humidity fluctuations are neglected and a climatic discretization based on inter-annual averages of the Bowen ratio (Bo is time-variable and fluctuate at shorter time scales). Since the correction tends to be small in semi-arid regions (recall that Bo is time-variable) Eq. (2.8) may be approximated as:

$$C_T^2 \approx \left(\frac{C_{n_{LAS}}^2 \overline{T}^4}{A_{T_{LAS}}^2 \overline{p}^2} \right) \tag{2.9}$$

Once C_T^2 is known, the sensible heat flux can be obtained according to the Monin-Obukhov Similarity Theory (MOST), iteratively from the following system of equations:

$$\frac{C_T^2 (Z_{LAS} - d)^{2/3}}{\theta_*^2} = f_T \left(\frac{Z_{LAS} - d}{L_{MO}} \right) = f_T(\zeta) \tag{2.10}$$

$$\theta_* = \frac{-H}{\rho c_p u_*} \tag{2.11}$$

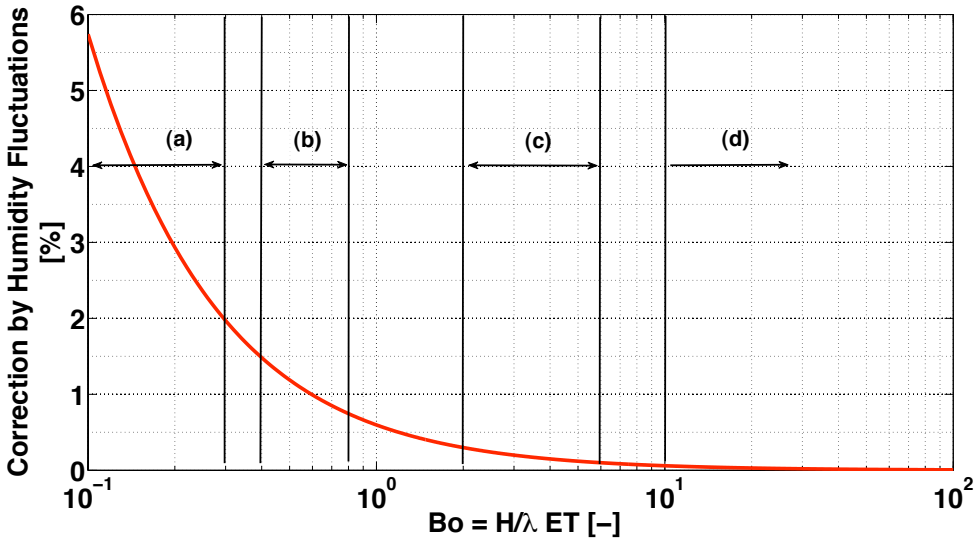

Figure 2.3: Correction to C_T^2 by humidity fluctuations in different climates. (a) Tropical rain forest, where high annual rainfall keeps soils wet year-round (1.97 -5.74%), (b) temperate forest and grasslands, where less rainfall causes drier soils (0.75-1.48 %), (c) semi-arid regions with dry soils (0.10-0.30 %), and (d) deserts (less than 0.06 %). Typical Bowen ratios for each climate where taken from Bonan (2002).

$$L_{MO} = \frac{u_*^2 T}{g\kappa\theta_*} \tag{2.12}$$

where Z_{LAS} is the LAS height, $f_T(\zeta) = c_1(1 - c_2\zeta)^{-2/3}$ and $f_T(\zeta) = c_1(1 - c_3\zeta^{2/3})$, with $\zeta = (Z_{LAS} - d)/L_{MO}$, are the universal stability function for unstable ($L_{MO} < 0$) and stable ($L_{MO} > 0$) conditions, respectively (Wyngaard et al., 1971; Andreas, 1988; De Bruin et al., 1993). θ_* is a temperature scale (virtual temperature), L_{MO} is the Obukhov length, $\kappa = 0.4$ is the von Karman constant and $c_1 = 4.9$, $c_2 = 6.1$, $c_3 = 2.2$.

The friction velocity u_* can be derived from wind speed data, u, mea-

sured at height z_u and estimates of the roughness length, z_0, zero displacement height, d, and stability correction functions introduced by Panofsky and Dutton (1984) (see Eq. (2.13)). There Ψ_m is the integrated stability function (Businger-Dyer correction) which takes into account the effect of thermally produced turbulence on momentum transport which generates non-adiabatic conditions.

$$u_* = \frac{\kappa u}{\ln\left(\frac{z_u - d}{z_0}\right) - \Psi_m\left(\frac{z_u - d}{L_{MO}}\right) + \Psi_m\left(\frac{z_0}{L_{MO}}\right)} \tag{2.13}$$

For unstable conditions (day-time):

$$\Psi_m\left(\frac{z}{L_{MO}}\right) = 2\ln\left(\frac{1+x}{2}\right) + \ln\left(\frac{1+x^2}{2}\right) - 2arctan(x) + \frac{\pi}{2} \tag{2.14}$$

with $x = (1 - 16z/L_{MO})^{1/4}$. And for stable conditions (night-time):

$$\Psi_m\left(\frac{z}{L_{MO}}\right) = -5\frac{z}{L_{MO}} \tag{2.15}$$

2.2 Instrumentation

Kipp & Zonen manufactures the Large Aperture Scintillometer (LAS) and eXtra Large Aperture Scintillometer (XLAS). They are designed for measuring the path-averaged structure parameter of the refractive index of air (C_n^2) over horizontal path lengths from 250 m to 4.5 km (LAS) and 1 km to 8 km

(XLAS). The light source of the LAS and XLAS transmitter operates at a near-infrared wavelength of 880 nm. At this wavelength, the observed scintillations are primarily caused by turbulent temperature fluctuations. Therefore, C_n^2 measurements obtained with the LAS or XLAS can be related to the sensible heat flux.

The LAS and XLAS feature heated transmitter and receiver windows and internal temperature monitoring, providing a mechanism to eliminate condensation problems. Modulation of the signal eliminates the background fluctuations in signal strength due to sunlight. Unlike mirror-based scintillometers, the Fresnel lense collimates and collects the light avoiding obstruction of the beam by the transmitting LED or the receiving detector. On-board calibration and reference signals at the receiver electronics allow rapid on-site confirmation of operation.

The instrument is eye-safe, operates on 12V DC power, and has built-in pan and tilt adjuster for easier alignment. The geometric aperture diameter is 0.152 m (as is the focal length), but the effective aperture diameter is 0.145 m for the receiver and 0.148 m for the transmitter. The power consumption of the transmitter varies from 2W at 1 km distance to 6W at 4.5 km distance, while the receiver draws 2.5 W.

Proper operation of the LAS requires setting the path length potentiometer which amplifies the voltage output for the proper gain. C_n^2 can then be easily obtained from the voltage output $U_{C_n^2}$ of the receiver using $C_n^2 = 10^{(U_{C_n^2} - 12)}$. The raw signal can also be saved using the demod differential voltage output which is proportional to the intensity of the signal I.

For data processing, the WINLAS software (Kipp & Zonen, 2007) is supplied to read in the LAS output data together with complementary meteorological data (wind speed and temperature) to obtain the sensible heat flux. The required parameters are wind speed measurement height, roughness length, displacement height, beam height, and Bowen ratio.

Scintec offers the BLS450, BLS900, and BLS2000. The BLS450 and BLS2000 are designed for applications with similar path lengths to the Kipp & Zonen LAS and XLAS, respectively. The BLS900 expands on the BLS450 and LAS by providing a dual beam setup. Transmitters 1 and 2 have different modulation frequencies allowing distinction of the beams by the receiver.

Unlike the LAS which has a Fresnel lens, with the BLS450 and BLS900 the beam is collimated by a plane convex lens (D=145 mm, focal length = 450 mm) onto 2 Si photodiodes with different sensitive areas. The BLS2000 uses a Fresnel lense of 265 mm diameter and a focal length of 495 mm. The main photodiode detector on the optical axis is used for sensing the turbulence-induced fluctuations of the received modulated pulses. After demodulation, the signals X and Y are available for the user during alignment. The auxiliary detector is used as an alignment aid. It provides the modulated signal Z.

The main advantage of the Scintec transmitters compared to the LAS transmitter is the larger emission angle. The BLS450 (LAS) has an emission half angle of 16° (0.6°) resulting in a beam width for a transect length of 1000 m of 287 m (10 m). This simplifies setup and alignment and improves the accuracy of C_n^2 during misalignment when the gradient in signal strength of the beam at the receiver in connection with scintillation (i.e. beam wandering) increases

the variance of the signal strength. It also makes the setup less sensitive to transmitter or tower vibrations. Moreover, the emission is more homogeneous due to a large number of radiation sources. The transmission can be pulsed at 1Hz - 125Hz providing the opportunity to select an optimum between power use of the transmitter (1-110W) and measurement accuracy.

Setup of a Scintec scintillometer transect can be accomplished by one person as the transmitter alignment can be done solely based on visual reference, while for the LAS a person standing at the LAS receiver has to radio the received beam intensity to the person aligning the transmitter. The Scintec BLS systems include a signal processing unit (SPU) which makes it a stand-alone package. The SPU does all the data processing and analysis, and provides basic error alerts. This simplifies the use of the scintillometer to obtain sensible heat fluxes, but it limits the options for modification to experts as no continuous raw data is provided. The LAS can easily be connected to any analog datalogger (supplied by the user) which allows easy integration of the complementary meteorological measurements (temperature, pressure, wind speed). Temperature and pressure sensors are sold as optional items by Scintec. The Scintec algorithm computes C_n^2 assuming free convective scaling for which no wind speed measurements are necessary. However, this assumption is often not justified. A rule of thumb is to not accept this assumption when $Z_{LAS}/L_{MO} > -0.3$. In that case, wind speed measurements are necessary to derive H using the approach used by the LAS.

Scintec uses the Clifford et al. (1974) algorithm to correct for saturation, which has been shown to yield accurate results (Kohsiek et al., 2006).

Output of both the corrected and uncorrected C_n^2 and H is provided, so that other corrections can be applied by the user. Kipp & Zonen suggests no saturation correction, but the manual suggests limits for the pathlength given heat flux and beam height.

Scintec's double beam scintillometers (BLS900 and BLS2000) have the advantage of a correction for absorption fluctuations, which cause changes of the received intensity due to changes of the transmissivity over the propagation path, for example, due to dust or light fog. This is different from changes of the received intensity due to scintillation caused by interference (focusing and defocusing) at temperature inhomogeneities. Absorption fluctuations may be falsely interpreted as scintillations, hence artificially increasing the derived measured heat flux. Because absorption fluctuations are caused by inhomogeneities which have a spatial scale on the order of the path length, the changes of the intensity due to absorption will be nearly identical and highly correlated over the two adjacent paths. Therefore, the magnitude of absorption fluctuations contributing to the log amplitude variances $B11$, $B22$ and $B12$ is nearly identical, and absorption fluctuations are eliminated by computing the corrected average log amplitude variance as $\sigma_{\ln(I)} = (B11 + B22)/2 - B12$. However, in rain or dense fog the strong beam attenuation will result in no received intensity and not permit scintillometer measurements. The double beam set up can also be exploited for the measurements of average crosswind speeds, but at the price of high power consumption of 60W at the maximum pulse setting of 125 Hz.

Apart from the need for 2 persons for the alignment, in practice the

Kipp & Zonen system is somewhat more intuitive to use as the lay-out of the alignment system is better and the analog signal meter on the back of the receiver gives a better indication of proper functionality. Both manufacturers are still optimizing their instrument. For example, Kipp & Zonen had problems with placing the LED in the focal of the lense in 2006. Scintec had issues with transmitter windows cracking due to improperly designed o-rings in 2007. These problems have been solved now but given the recent market entry for the scintillometers, more problems are likely to appear for both manufacturers in the near future.

CHAPTER 3

MATERIALS AND METHODS

3.1 New Mexico Scintillometer Network (NM-LASNet)

The scintillometer network in New Mexico (hereafter, NM-LASNet) is located within and around the Middle Rio Grande Basin. It consists of seven Kipp & Zonen Large Aperture Scintillometer (LAS) transects at different locations representing a range of elevations (1448 - 2658 m) and land surfaces. For the purpose of this thesis the five most representative sites will be used: (i) San Acacia Alfalfa (SAA) which is a homogeneous irrigated alfalfa field, (ii) San Acacia Riparian (SAR) which is a heterogeneous moist riparian area, (iii) El Malpais National Monument (EMNM) which is a homogeneous basalt outcrop, (iv) Sevilleta National Wildlife Refuge (SNWR) which is a dry homogeneous shrubland, and (v) Valles Caldera National Preserve (VCNP) which is a moist homogeneous grassland. Figs. 3.1 and 3.2 show the location and photographs of the transects used in the study, Fig. 3.3 shows the topography of the transects. Terrain elevation changes are used to raise the beam height, leading to slanted and irregular surfaces. Finally, Table 3.1 has a description of each transect and the main parameters and sensors used in the estimation of sensible heat fluxes.

Before the set-ups were in their current locations, Kleissl et al. (2008) conducted an intercomparison study to quantify the accuracy of sensible heat flux measurements from LAS by comparing data from one EC system and up

to five adjacent scintillometer transects over homogeneous grassland areas in SNWR and VCNP. By varying the effective beam height, transect distance, and averaging time, the effect of these parameters on measurement accuracy was examined. The data showed agreement to typically $\pm 9\%$ between the sensible heat fluxes measured with different LASs.

The two principal objectives for our current scintillometer network are: (1) Develop efficient operating procedures and wireless infrastructure for the operation of scintillometers over a large region; and (2) Develop procedures for the use of sensible heat flux measurements by scintillometers for the calibration and validation of remote sensing algorithms. Only after these protocols and procedures have been developed, can we install a more permanent network for operational purposes in New Mexico.

A permanent network of scintillometers will provide H ground-truth data around the state. This data, in an operational basis, has important applications: (i) validation and calibration of regional remote sensing estimations of turbulent heat fluxes and (ii) hydrologic prediction.

This data impose constrains that may be used to obtain better nearly real-time estimates of evapotranspiration, based on validation procedures, and estimate the error of the evapotranspiration maps, offering a better product to the community. The availability of nearly real-time regional maps of evapotranspiration has important implications for agricultural water management since they can be used to improve irrigation scheduling and reservoir storage optimization.

On the other hand, scintillometer data become an important constrain

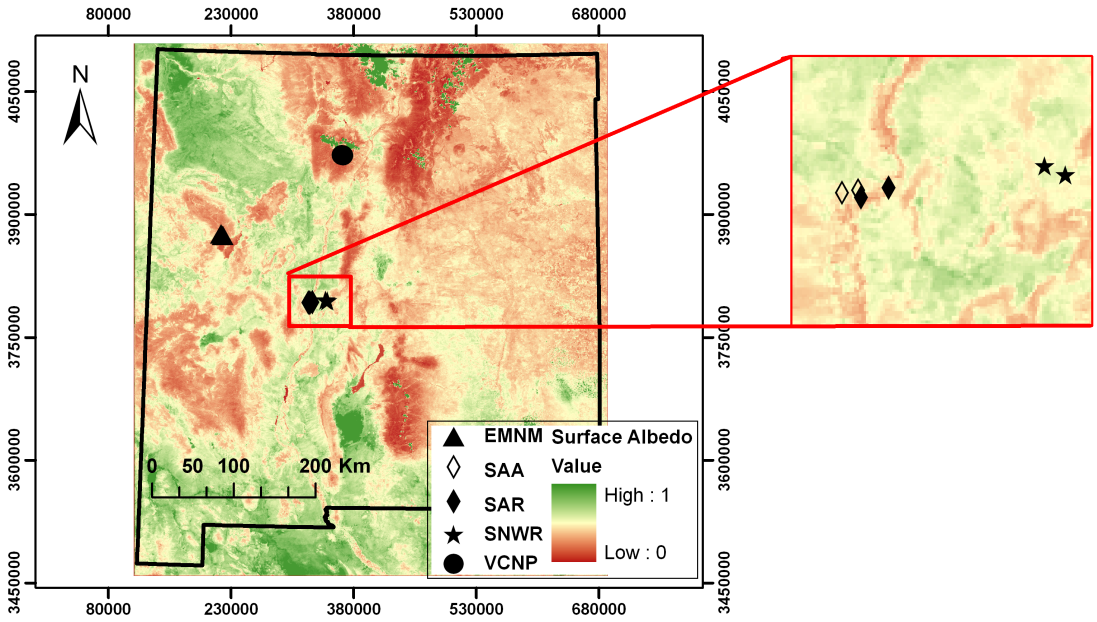

Figure 3.1: Locations of LAS transects in New Mexico (the transect consist of transmitter and receiver). The surface albedo map was generated with SEBAL in June 16 of 2002.

for lumped and distributed hydrological models that predict the components of the surface energy balance. In a continuous fashion, it may be used for data assimilation, improving real-time prediction, or for validation and calibration purposes. Although this ground-truth data is not available everywhere, maps of evapotranspiration and sensible heat fluxes, previously validated and calibrated, can be used for hydrological modeling.

3.2 Intercomparison Experiment Set-up

As part of the intercomparison experiment conducted by Kleissl et al. (2008), sensible heat flux, net radiation and ground heat flux were measured at Sevilleta (SNWR) and Valles Caldera (VCNP), from January 18 to February

Table 3.1: NM-LASNet. All locations are given in UTM 13 (WGS 84), unless otherwise noted. z_o: roughness length, d: zero displacement height. Meteorological sensors: R_{sd}: shortwave downwelling radiation, $wspd$: wind speed, $wdir$: wind direction, T: Temperature, RH: relative humidity, T_{sfc}: IR surface temperature, EC/EB: Eddy covariance/Energy balance, soil: soil temperature, moisture, conductivity at 0.1 m.

Site	**SAA**	**SAR**	**EMNM**	**SNWR**	**VCNP**
Ecosystem	Alfalfa	Riparian	Lava Flows	Dry Grassland	Mountains Grassland
	(homogen.)	(heterogen.)	(homogen.)	(homogen.)	(homogen.)
z_0 / d **[m]**	variable	0.31 / 4.14	0.2 / 0.1	0.026 / 0.01	0.014 / 0.01
LAS Serial No.	050017	050024	060031	050016	060032
Data Since	9-Sep-06	3-May-06	1-Sep-06	19-Nov-05	6-Jun-06
Receiver			(UTM 12)		
Northing [m]	3792556	3791818	3876026	3795105	3972272
Easting [m]	326121	326400	765019	345711	367312
Elevation [m]	1460	1486	2533	1688	2674.82
Transmitter			(UTM 12)		
Northing [m]	3792296	3792843	3874340	3794128	3972872
Easting [m]	324409	329312	767611	347899	365401
Elevation [m]	1424	1472	2423	1789	2677.74
Meteorological Station					
Northing [m]	37928146	34.265602 $°N$	3875505	At receiver	3969278
Easting [m]	324999	-106.86776 $°W$	766108		362649
Elevation [m]	1429	1427	2395		2658
Meteorological	T_{sfc}, $wspd$	R_{sd}, $wspd$	R_{net}, T/RH(2m)	R_{sd}, $wspd$	R_{sd}, $wspd$
Sensors	$wdir$, T/RH	$wdir$, T	$wspd$, $wdir$	$wdir$, T/RH	$wdir$, T/RH
	T_{soil}, $rain$	T_{sfc}	R_{sd}, T_{sfc}	T_{sfc}	R_{sd}, $soil$
		EC/EB tower	T(0.1m)		EC/EB tower
L [m]	1732	3087	2941	2398	2003
Z_{eff} **[m]**	20	44.8	59.8	31.5	42.6

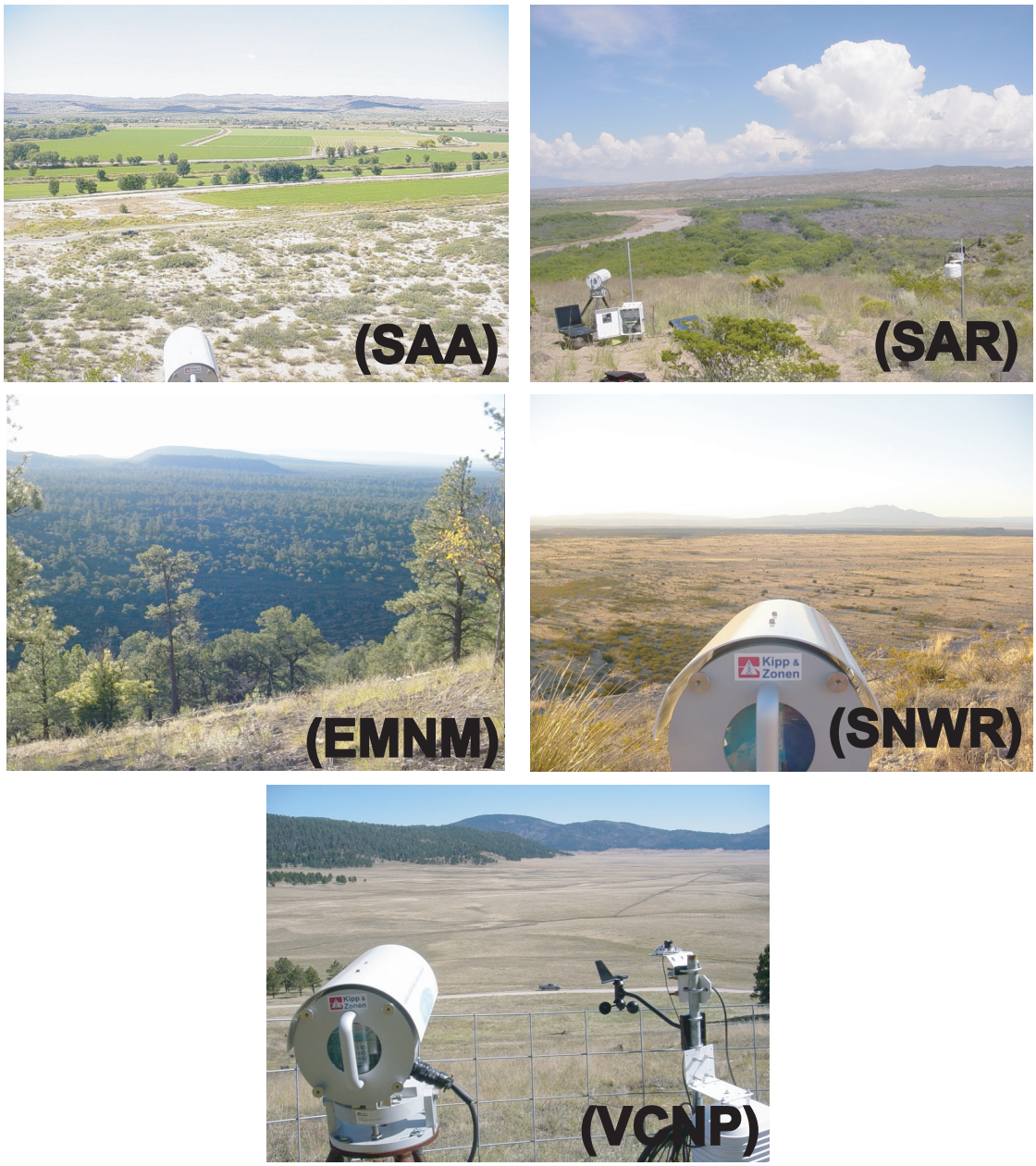

Figure 3.2: LAS setup locations in New Mexico: San Acacia alfalfa crop (SAA), San Acacia riparian area (SAR), El Malpais basalt outcrops (EMNM), Sevilleta National Wildlife Refuge (SNWR), and Valles Caldera mountainous grassland (VCNP).

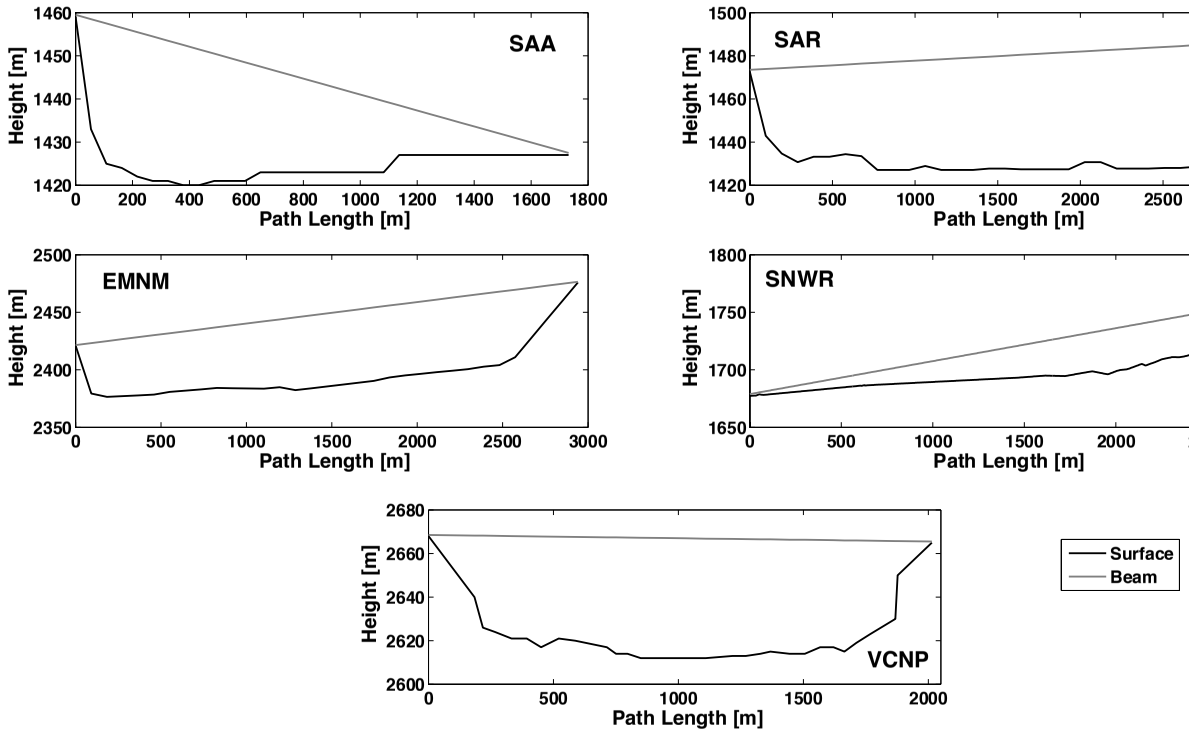

Figure 3.3: Topographic characteristics of LAS transects in New Mexico. Scintillometer beam elevation Z_{beam} (gray line), surface elevation Z_{sfc} (black line). The scintillometer beam height, along the path x, can be estimated as $Z_{LAS}(x) = Z_{beam} - Z_{sfc}$.

8 of 2006 and from June 8 to June 25 of 2006, respectively.

At the SNWR and during the experiment, mean daily maximum and minimum air temperatures were 14.8 $^{\circ}C$ and -3.4 $^{\circ}C$, respectively. The network of weather stations, managed by the Sevilleta Long-Term Ecological Research Project, detected a small rainfall event of about 1.3 mm on January 25. During the rest of the experiment, no additional rainfall was present. The LAS transmitter was located on a ridge and the receiver was set up 80 m lower in the plains at a bearing of $\sim$ 295 degrees from the receiver, resulting in an slanted path (see figure 3.3). The path length was 2713 m and the topographic profile and beam height were established with waypoints taken with a GPS with Wide Area Augmentation System (GPS-WAAS). The absolute accuracy of GPS-WAAS is $\sim$ 1 m or 6% of the beam height. An eddy covariance tower was located at the center of the transect and was used to estimate the sensible heat fluxes (no latent heat flux was measured). Based on the methodology proposed by Martano (2000), sonic anemometer measurements were used to estimate the roughness length (z_0 = 0.026 m) and zero displacement height (d = 0.01 m).

At the VCNP and during the experiment, mean daily maximum and minimum air temperatures were 23.6 $^{\circ}C$ and 4.4 $^{\circ}C$, respectively. Only 1.5 mm of rain was recorded between May 19 and June 6, 2006. June was relatively dry with the only rainfall occurring between June 6 and June 9 (16 mm) and between June 24 and June 28 (25.2 mm). The monsoon season started in July, after the end of the experiment. The LAS was elevated on two slopes which overlook relatively flat grassland (see Fig. 3.3). The path length was 2019 m

and the topographic profile and beam height were established with two hundred waypoints taken with a GPS-WAAS. The absolute accuracy of GPS-WAAS is $\sim$ 1 m or 2% of the beam height. Also, special care was taken to accurately determine the relative height of the transmitter and receiver with a differential GPS (DGPS). Finally, an eddy covariance tower was located 1.3 km south of the transect over homogeneous grassland (grass height 0.3-0.5 m) similar to the vegetation in the footprint of the LAS. From this station, sensible and latent heat fluxes were estimated, however the latent heat fluxes were corrupted due to malfunctioning on the system. Based on the methodology proposed by Martano (2000), sonic anemometer measurements were used to estimate the roughness length ($z_0 = 0.014$ m) and zero displacement height ($d = 0.01$ m). All instrumentation used during the intercomparison experiment is in Table 3.2.

3.3 Saturation Experiment Set-up

If turbulence becomes too intense, the measured intensity fluctuations of the scintillations $\sigma^2_{\ln(I)}$ increase above a certain level, and they are no longer proportional to C_n^2 (see Eq. (2.4)) which results in an underestimation of H (Clifford et al., 1974). This phenomenon is known saturation.

To study saturation of the LAS signal, the University of Wageningen and New Mexico Tech conducted an experiment during the summer of 2007. It consisted of a set-up of two LASs (Kipp & Zonen), one XLAS (Kipp & Zonen), one BLS450 (Scintec), and one EC station. The aperture of the XLAS is twice that of the LAS, enabling use over distances of up to 10 km (Kohsiek et al., 2002), being more resistant to saturation. In one of the experimental set-up,

Table 3.2: Instrumentation for the intercomparison experiment.

Site	**SNWR**	**VCNP**
EC tower		
Location	Near the center of the transect	1.3 km south of the transect
Measured	H, R_n, G	H, R_n, G
Datalogger	CR10X (Campbell Scientific) (10 min avg)	CR5000 (Campbell Scientific) (30 min avg)
For H	CSAT3 (u, v, w) at 2.85 m AGL Sampling rate 8 Hz (Campbell Scientific)	CSAT3 (u, v, w) at 2.85 m AGL Sampling rate 20 Hz (Campbell Scientific)
For R_n	REBS Q7 at 2.7 m AGL (Campbell Scientific)	NR-Lite net radiometer at 2.7 m AGL (Kipp & Zonen)
For G	Hukseflux self-calibrationg heat flux plate at -6 cm	Two soil heat flux plates
Other	Thermocouple (soil temperature at -3 cm)	Licor 7500 open path CO_2/H_2O IRGA Vaisala HMP45C temperature/humidity probe Two pyranometers Soil water content reflectometers (-5 cm and -15 cm) Tipping bucket rain gauge
LAS transects		
Measured	H	H
Datalogger	CR10X (Campbell Scientific) (10 min avg)	CR10X (Campbell Scientific) (10 min avg)
For H	LAS (Kipp & Zonen) Sampling rate 1 Hz L = 2751 m	LAS (Kipp & Zonen) Sampling rate 1 Hz L = 2019 m

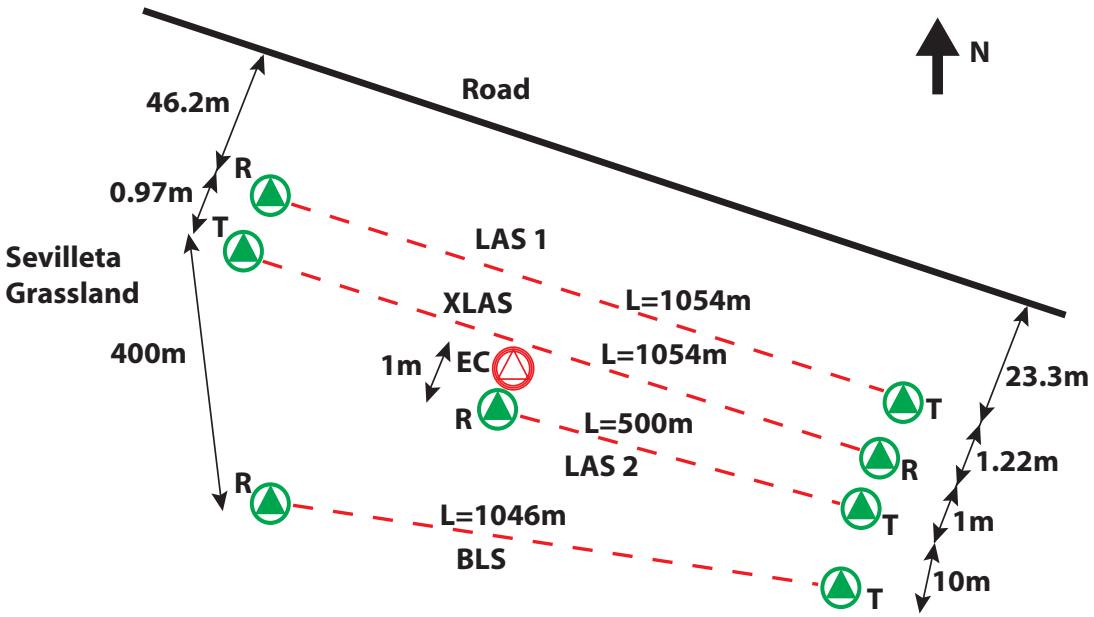

Figure 3.4: Sketch of the saturation set-up. T stands for transmitter and R for receiver.

one LAS (LAS 1) and one XLAS were located in a homogeneous and almost flat surface with a path length of 1054 m and a height of 1.5 m; the other LAS (LAS 2) was on the same place (close enough to avoid signal cross-contamination) and at the same height, but with a path length of 500 m. A sketch of the set-up is showed in Fig. 3.4.

The purpose of this experiment was to observe saturation in the LAS 1, while the XLAS and LAS 2 were operating properly. The data collected will be used to test available methods for the correction of saturation (Kohsiek et al., 2006) and the development of new ones. This work will be part of a coming publication.

CHAPTER 4

SCINTILLOMETER MEASUREMENTS AND DATA ANALYSIS

4.1 Instrument Set-up and Operation

The optimal transect for a LAS is placed perpendicular to the predominant wind direction to have maximum source area (Meijninger et al., 2002) and parallel to the earth's surface (i.e. horizontal). It should also follow a north-south orientation to avoid exposure and possible damage of the optical parts by direct sunlight under low sun angles (Kipp & Zonen, 2007). The ideal height of the beam above the land surface depends on the depth of the constant flux layer where the Monin-Obukhov Similarity Theory (MOST) can be applied which is needed for derivation of H from C_T^2 (Eqs. (2.5)-(2.13)). The constant flux layer overlays the roughness sub-layer which is influenced by the structure of the roughness elements on the land surface (e.g. plants, trees, buildings, etc.). The top of the roughness sub-layer corresponds with the lower level of the constant flux layer; it is the minimum height above the land surface for the scintillometer beam and is estimated as three times the height of the obstacles on the land surface (Oke, 1987). Thus, the minimum height for a LAS is 1.5 m over grassland and shallow shrubs but it will be considerably higher for trees (Kipp & Zonen, 2007). The maximum height is the top of the constant flux layer, which is on the order of 200 m in daytime, and 10s of meters at night (Stull, 1988).

The minimum height is not only determined by the height of the roughness sub-layer, but also by the phenomenon of saturation which is explained in section 4.4.

Another challenge is to find a LAS transect where the laser beam is horizontal to the land surface, especially when one needs measurements on the scale of a MODIS (250 m) or AVHRR (30 m) pixel, i.e. transects much larger than both MODIS/AVHRR. The construction of towers with a height exceeding 10 or 20 m is an option and indeed is a common approach for eddy covariance measurements above forests (Schellekens et al., 2000). However, towers for LASs need to be stiff since any vibration in the tower generated by wind will be interpreted by the scintillometer as an increase in scintillations. Therefore, LAS towers will be more expensive than the towers often used for meteorological measurements. An alternative is to search for two hills a few kms apart or to measure over valleys (Hafeez et al., 2007; Meijninger and De Bruin, 2000). Where such landscape features cannot be found, an alternative is to put the scintillometers over a slanted path (Fig. 3.3). This is a common situation for many hydrological studies and results in scintillometer beam heights that vary along the path. This also means that the scintillometer measurements not only represent a horizontal but also a vertical average of C_T^2 (see section 4.3). In this case, the average height of transmitter and receiver does not represent the height of the vertically averaged C_T^2, because C_T^2 does not vary linearly with height, and the scintillometer signal is weighted towards the middle of the path.

The obvious advantage of the slanted paths is a substantial reduction

in costs for each transect since the construction of stiff towers is expensive. Another advantage is that it allows establishing rather long transects from 2000 to 3000 m at effective heights of 30 to 60 m that avoid saturation. The disadvantage is a larger uncertainty in the derived sensible heat fluxes H (see section 4.3). While uncertainty in the physical height of the beam over the transect can be eliminated by careful elevation measurements using differential GPS, the uncertainty caused by different methods for determining the effective height remains. This issue may also affect the onset of saturation and requires more research (Hartogensis et al., 2003).

4.2 Stable and Unstable Atmospheric Conditions

As discussed before (see chapter 2), the turbulent behavior of the atmospheric boundary layer (ABL) can be envisioned as a collection of eddies of different sizes, where large eddies progressively break down into smaller eddies (cascade process) and, at the same time, transfer kinetic energy from larger to smaller eddies. Much of the energy necessary to generate this turbulent flow comes from forcings at the ground, for example, solar heating of the ground causes thermals of warmer air to rise, generating large eddies (thermally induced turbulence - TIT) or frictional drag on the air flowing over the ground causes wind shears to develop, which frequently become turbulence (mechanically induced turbulence - MIT). Turbulence is several orders of magnitude more effective at transporting quantities that molecular diffusion (e.g. H, λET, CO_2, etc.), and usually TIT is stronger than MIT.

The transport of energy within the earth-atmosphere system is possible in three modes: conduction (for G), radiation (for R_n), and convection

(for H and λET). Particularly, convection can be classified as free (caused by TIT), forced (caused by MIT), or mixed (cause by both MIT and TIT). When the surface is heated by solar radiation (temperature decreases with elevation), parcels of air close to the surface tend to raise, then free convection is enhanced and the atmosphere is said to be unstable ($H > 0$ and $L_{MO} < 0$). On the other hand, if the soil is colder than the surrounding air, parcels of air tend to sink, then free convection is inhibited, and the atmosphere is said to be stable ($H < 0$ and $L_{MO} < 0$). If there is not tendency of the air parcels to rise or sink (environmental lapse rate is equal to adiabatic lapse rate (see (Oke, 1987) for a definition)), the atmosphere is in neutral conditions.

Usually, the atmosphere is stable during the night (approximately between sunset and sunrise) and unstable during the day, when solar radiation heats the surface (approximately between sunrise and sunset). However, overcast conditions or advection of heat from the surroundings may decrease H during the day, and even suppress the TIT, causing stable conditions ($H < 0$). Between the change from stable to unstable and unstable to stable conditions, the atmosphere experiences neutral conditions.

The LAS relates the variability of scintillations in the turbulent atmosphere with the strength of the mixed convection, but does not measure the temperature gradient. Therefore, it cannot infer the direction of the heat flux. At first one stable and one unstable solution are derived for each time interval using the MOST, however, the atmospheric conditions are necessary in order to decide which solution to use.

A distinct minima in C_n^2 can be used to infer the location of neutral

conditions and stable-unstable and unstable-stable transitions (see Fig. 4.1). The tracking of neutral conditions, for a sunny and calm day (as in Fig. 4.1), can be easily implemented in an algorithm, but it may not be possible in other cases. As a result, a careful analysis of the diurnal cycle of C_n^2 has to be done each day in order to choose an adequate solution. A more accurate approach is to have measurements of air temperature at two heights (e.g. $z_1 = 0.1$ m and $z_2 = 2$ m), then using the temperature gradient ($\Delta T/\Delta z = (T_1 - T_2)/(z_1 - z_2)$) as a proxy for flux direction. In this case positive values of the gradient will mean negative H and stable atmospheric conditions. The measurement of ΔT is recommended where irrigated fields or riparian areas will be exposed to advective lateral energy fluxes.

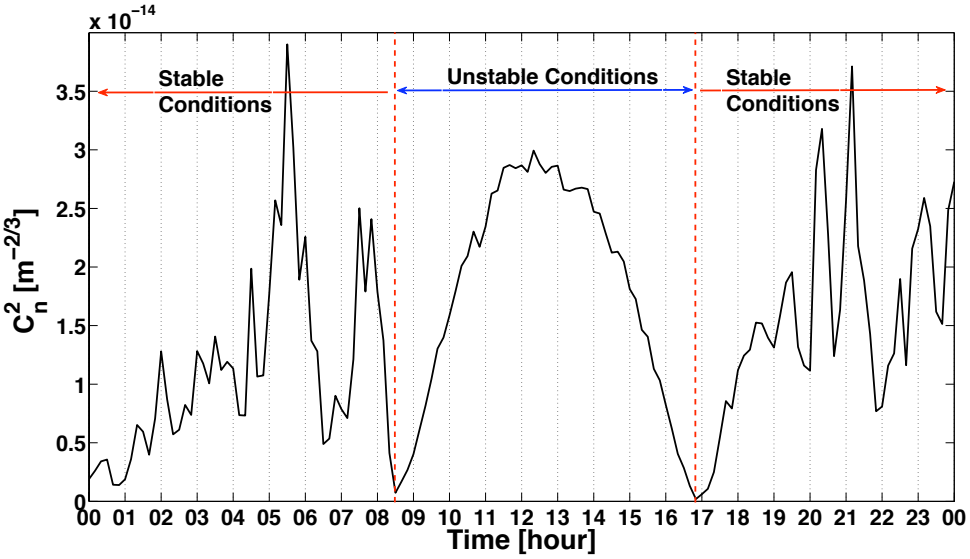

Figure 4.1: Example of diurnal cycle of C_n^2 obtained with a LAS for a sunny day at the Sevilleta National Wildlife Refuge LAS transect on February 3, 2006. Note the steep drop in C_n^2 when atmospheric stability changes from stable to unstable and back to stable.

4.3 The Effective Beam Height

The scintillation method (Eqs. (2.5)-(2.13)) is based on a unique value of Z_{LAS}. However, in practical applications, the LAS beam height often varies along the path due to sloping terrain, difference of installation heights of transmitter and receiver, or even variations of the Earth's curvature. Fig. 3.3 shows five particular cases where the absence of ideal terrain conditions leads to set-ups over irregular surfaces and slanted paths.

Under these non-ideal circumstances, the LAS measurements represent both horizontal and vertical averages of the structure parameter of temperature (C_T^2). A simple average height between transmitter and receiver is then not representative of the average C_T^2, since it varies non-linearly with height and the scintillometer sensitivity is weighted towards the center of the path (Wang et al., 1978). Taking into account the cascade process in the turbulent boundary layer, it is expected that the spatial variability of temperature (quantified by C_T^2) will be a function of the eddy size involved in the transport of kinetic energy; and therefore, of the height. Wyngaard et al. (1971), demonstrated that, within the mixing layer, C_T^2 can be calculated as:

$$C_T^2 = 2.68\left(\frac{g}{T}\right)^{-2/3}\left(\frac{z}{\overline{w'T'}}\right)^{-4/3} \tag{4.1}$$

where g is gravity acceleration, T is air temperature, z is height, and $\overline{w'T'}$ is the covariance of vertical wind direction and temperature.

Hartogensis et al. (2003) derived Eq. (4.2) to calculate an effective height (Z_{eff}) to use in situations where the LAS beam height varies along the

path. This effective height is used in the derivation of sensible heat fluxes (Eqs. (2.5)-(2.13)).

$$Z_{eff}^{-2/3} f_T\left(\frac{Z_{eff}}{L_{MO}}\right) = \int_0^1 Z(x')^{-2/3} f_T\left(\frac{Z_{eff}}{L_{MO}}\right) G(x')dx' \tag{4.2}$$

$$G(x') = \frac{W(x')}{\int_0^1 W(x')dx'} \tag{4.3}$$

where $f_T(\zeta) = c_1(1 - c_2\zeta)^{-2/3}$ and $f_T(\zeta) = c_1(1 - c_3\zeta^{2/3})$, with $\zeta = (Z_{LAS} - d)/L_{MO}$, are the universal stability function for unstable ($L_{MO} < 0$) and stable ($L_{MO} > 0$) conditions, respectively (Wyngaard et al., 1971; Andreas, 1988; De Bruin et al., 1993). The effective height Z_{eff} depends on atmospheric stability and is solved iteratively in conjunction with θ^* and u^* in order to estimate H, resulting in a different Z_{eff} for each averaging interval (Hartogensis et al., 2003).

The fundamental assumption for Eq. (4.2) is the presence of a constant flux layer which means that C_T^2 is in equilibrium with the surface. While this is always the case for homogeneous and flat surfaces, this assumption also holds for heterogeneous surfaces as long as the measurements are taken at a level above the internal boundary layer of the heterogeneous patches - the blending height - , where the individual patch signatures merge due to turbulent mixing (Meijninger et al., 2002). Accurate determination of the effective height is critical since a relative error in Z_{eff} will result in at least half that relative error in H. Andreas (1989) derived the following expression to estimate the relative error in H due to a relative error in Z_{eff} as a function of stability

$$\frac{\delta H/H}{\delta Z_{eff}/Z_{eff}} = \frac{1}{2}\left(\frac{1 - 2c_2\frac{Z_{eff}}{L_{MO}}}{1 - c_2\frac{Z_{eff}}{L_{MO}}}\right) \tag{4.4}$$

where δH is the error in H, δZ_{eff} is the error in Z_{eff}, and c_2 is the constant of the universal function of stability ($c_2 = 6.1$). For free convection conditions ($Z_{eff}/L_{MO} \rightarrow \infty$), a relative error in Z_{eff} causes an equal relative error in H. For neutral conditions ($Z_{eff}/L_{MO} \rightarrow 0$), on the other hand, the relative error in H due to Z_{eff} is half the relative error in Z_{eff}. These are extreme conditions, then the relative errors for stable and unstable conditions are in between.

4.4 Saturation

Eq. (2.4) is based on first-order scattering theory (i.e. the wave is scattered only once), therefore, it is only valid in a weak scattering medium. If the turbulence becomes too intense (i.e. a strong scattering medium where scattering occurs more than once), the measured intensity fluctuations of the scintillations $\sigma^2_{\ln(I)}$ increase above a certain level, and they are no longer proportional to C_n^2 (see Eq. (2.4)) which results in an underestimation of H (Clifford et al., 1974).

A criterion for saturation-free conditions is $C_n^2 < 0.185 D^{5/3}\lambda^{1/3}L^{-8/3}$ (Ochs and Hill, 1982). Note that C_n^2 is not only a function of path length L, but also of height of the laser beam above the land surface Z_{eff} (see Eq. (2.10)); the larger Z_{eff} the less intense the scintillations. Since aperture diameter D and wave length λ are instrument constants, Z_{eff} and L determine whether saturation occurs (Hartogensis et al., 2003). In general, the longer the path,

the higher the LAS needs to be installed to avoid saturation. The LAS manual provides graphics to quickly determine the minimum installation height of the LAS as a function of path length and for different values of the sensible heat flux (Kipp & Zonen, 2007). For example, to measure a sensible heat flux of 400 Wm^{-2} (common in New Mexico) over a path length of 2750 m, the height of the LAS must be 30 m, whereas a sensible heat flux of 200 Wm^{-2} would require a height of 10 m. Consequently, large installation heights must be chosen in arid and semi-arid regions since sensible heat fluxes are generally high.

Using the configuration of the saturation set-up, described in section 3.3, saturation is expected to occur for large sensible heat flux, and therefore very strong turbulent conditions will affect the measurements in LAS 1, but not in XLAS and LAS 2 (less susceptible to saturation due to its short transect). Fig. 4.2 shows that C_n^2 of LAS 1 deviates significantly from XLAS for large C_n^2, demonstrating the presence of saturation in LAS 1, leading to underestimation of sensible heat fluxes.

4.5 The Footprint

The footprint of a turbulent flux measurement defines the spatial extent of the measurement (Schmid, 2002). The flux measured by a turbulent flux sensor reflects the influence of the underlying surface on the turbulent exchange. When the instruments are deployed over a homogeneous surface, the exact location of the instrument is not an issue, because the fluxes from all parts of the surface are by definition equal. However, if the surface is heterogeneous (e.g. most natural land covers and urban areas), the measured signal is dominated by the surface that has the strongest influence on the sensor,

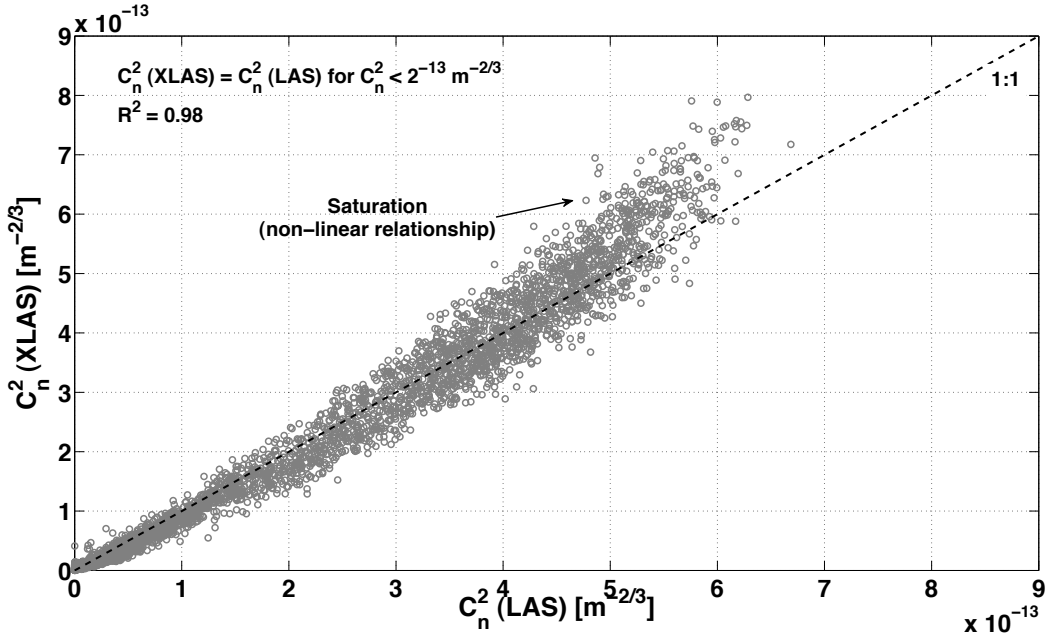

Figure 4.2: Comparison of C_n^2 for a LAS and XLAS during the saturation experiment at Sevilleta National Wildlife Refuge (July 14-17, 2007). The C_n^2 (LAS) levels off at large C_n^2 indicating saturation.

and thus on the location and size of the footprint matter (Schmid, 2002).

The footprint function describes the relative contribution of each surface source, per unit source strength, per unit element, to the measured scalar flux. Pasquill and Smith (1983) proposed a formal mathematical expression:

$$\eta(\mathbf{r}) = \int_{\Re} Q_\eta(\mathbf{r}+\mathbf{r}')f(\mathbf{r},\mathbf{r}')d\mathbf{r}', \tag{4.5}$$

where η is the measured value at location $\mathbf{r}$, $Q_\eta(\mathbf{r}+\mathbf{r}')$ is the distribution of source (e.g. sensible heat flux release under unstable atmospheric conditions) or sink (e.g. CO_2 assimilation by vegetation during the day) strength in the

surface-vegetation volume, and $f(\mathbf{r}, \mathbf{r}')$ is the footprint or transfer function, depending on $\mathbf{r}$, and on the separation between measurement and forcing, $\mathbf{r}'$. The integration is performed over the domain $\Re$.

One common simplification to Eq. (4.5), which is used by the majority of current footprint models, is the inverted plume assumption (Pasquill, 1972). This assumption implies that the footprint function, f, is independent of the sensor location, $\mathbf{r}$, and therefore of the source or sink strength, $Q_\eta(\mathbf{r}+\mathbf{r}')$, thus $f(\mathbf{r}, \mathbf{r}') \approx f(\mathbf{r}')$. However, this assumption may be invalidated by growth of internal boundary layers in response to step-changes in the thermal (variations in bouyancy production) or mechanical (distribution of momentum sinks due to patchiness) surface forcing.

Nevertheless, the inverted plume assumption is considered valid in areas where the spatial inhomogeneities are primary due to variations in the source or sink strength of passive scalars, and any variations in mechanical or thermal turbulence production are confined to small length scales, compared to the reference height of footprint considerations (Schmid, 2002).

The footprint estimation has had three main approaches: (i) Eulerian analytical solutions to the advection-diffusion equation (Horst, 1999; Finn et al., 1996; Horst and Weil, 1994, 1992; Gash, 1986), (ii) forward and backward Lagrangian stochastic simulations (Kljun et al., 2002; Reynolds, 1998; Rotach et al., 1996; Rodean, 1996; Wilson and Sawford, 1996; Flesch et al., 1995), and (iii) large-eddy simulations (LES) (Leclerc et al., 1997; Hadfield, 1994). All of them are limited by assumptions in their development, which are usually more restrictive in the case of the analytical solutions. Schmid (2002) has reviewed

of the most common methods, assumptions, and limitations.

For the purpose of this paper, we used the model proposed by Hsieh et al. (2000) (henceforth, the HKC). It is an hybrid approach which uses results of a Lagrangian footprint model to parameterize an analytical model and overcome the computational demand of more complex models and limitations in the assumptions of pure analytic models. Mathematically, flux and footprint are defined by:

$$\eta(x, z_m) = \int_{-\infty}^{x} Q_\eta(x) f(x, z_m) dx, \tag{4.6}$$

where η is the scalar flux $[gm^{-2}s^{-1}]$, f $[m^{-1}]$ is the footprint, Q_η $[gm^{-2}s^{-1}]$ is the source strength (or termed as surface flux), z_m $[m]$ is the measurement height, and the mean wind direction is along the horizontal coordinate x.

A homogeneous velocity field with scalar source strength is assumed, however it may be wrong for a heterogeneous surface. The functional form of the strength source is:

$$Q_\eta(x) = \begin{cases} 0 & for\ x < 0, \\ S_0 & for\ x \geqslant 0. \end{cases} \tag{4.7}$$

Then, the flux can be estimated by:

$$\frac{\eta(x, z_m)}{S_0} = \exp\left(\frac{-1}{\kappa^2 x} D z_s^P |L_{MO}|^{1-P}\right), \tag{4.8}$$

and the footprint by:

$$f(x, z_m) = \frac{1}{S_0}\frac{d\eta(x, z_m)}{dx} = \frac{1}{\kappa^2 x^2} D z_s^P |L_{MO}|^{1-P} \exp\left(\frac{-1}{\kappa^2 x} D z_s^P |L_{MO}|^{1-P}\right), \tag{4.9}$$

where D and P are similarity constants estimated from regression analysis between the dimensionless groups x/L_{MO} and z_s/L_{MO}, with the first one obtained from the Lagrangian model proposed by Thomson (1987). These constants depend on atmospheric stability: (i) unstable ($D = 0.28$ and $P = 0.59$), (ii) near neutral ($|z_s/L_{MO}| < 0.04$) and neutral ($D = 0.97$ and $P = 1$), and (iii) stable ($D = 2.44$ and $P = 1.33$). The variable z_s is a length scale defined as:

$$z_s = z_m\left(\ln\left(\frac{z_m}{z_0}\right) - 1 + \frac{z_0}{z_m}\right). \tag{4.10}$$

This model analytically relates atmospheric stability (L_{MO}), measurement height (z_m), and surface roughness length (z_0) to flux and footprint in thermally stratified atmospheric surface layer flows.

Since the HKC model is describing the footprint along the mean wind direction (i.e. two-dimensional in the z-x axis), a lateral dispersion model is necessary in order to get a three-dimensional representation. In this study, the model proposed by Gryning et al. (1987) is used. This approach describes the lateral dispersion as a process caused exclusively by turbulence of the air, neglecting the effects of shear in the wind direction which may become more important under very unstable conditions. Assuming the lateral plume profile has a Gaussian distribution, the transfer function can be calculated at the surface at any point using:

$$f_{3D}(x, y, z_m) = \frac{f(x, z_m)}{(2\pi)^{1/2}\sigma_y} \exp\left(- \frac{y^2}{2\sigma_y^2} \right) \tag{4.11}$$

where y is the crosswind distance [m] and σ_y is the crosswind spread of the plume [m]. The crosswind spread of the plume is estimated as (Gryning et al., 1987)

$$\sigma_y = \sigma_v t f_v \left(\frac{t}{T_y} \right) \tag{4.12}$$

where σ_v is the standard deviation of the lateral wind fluctuations, f_v is a empirical function of the dimensionless travel time t/T_y and T_y is the Lagrangian time scale for the lateral dispersion. Weber (1998) has a detailed description of the different methods for the estimation of σ_v. In this study, we used the simple linear approximation (small-angle approximation) showed in Eq. (4.13), relating the standard deviation σ_θ (in radians) of horizontal wind direction with the the mean longitudinal wind speed $\overline{u}$ (the vector mean).

$$\sigma_v \approx \overline{u}\sigma_\theta. \tag{4.13}$$

It is important to take into account the difference between the value reported by a cup anemometer (u), which is the scalar mean wind speed and the value $\overline{u}$ in Eq. (4.13). However, the approximation $\overline{u} \approx u$ is used.

The function f_v can be estimated according to Draxler (1976) as:

$$f_v \left(\frac{t}{T_y} \right) = \frac{1}{\left(1 + \left(\frac{t}{2T_y} \right)^{1/2} \right)}, \tag{4.14}$$

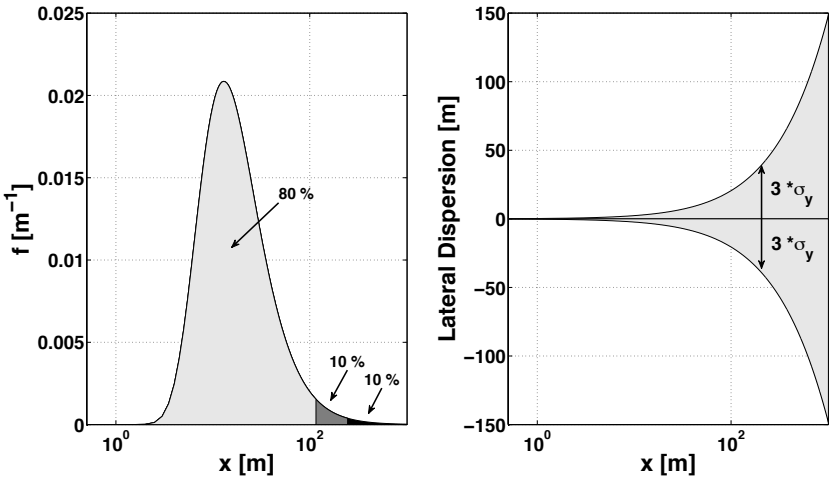

Figure 4.3: Example of a one-dimensional footprint with the HKC-model (left) and the lateral dispersion in the cross-wind direction (right). Assuming a normal distribution (see Eq. (4.11)), 99.8% of the lateral fluxes are between $3\sigma_y$.

where $t = x/\overline{u}$ (for $\overline{u}$ constant in space and time) and $T_y = 600$ s for elevated sources or $T_y = 200$ s for ground level sources. Then, from the practical point of view, $\overline{u}$ can be estimated from a cup anemometer and σ_θ is usually measured and stored, but it can also be estimated using the Yamartino algorithm (Yamartino, 1984) (not showed).

Fig. 4.3 shows an example of the HKC-model shape on the downwind direction (x) and the lateral dispersion component in the cross-wind direction (Eq. (4.12)). The combination of both processes leads the three-dimensional footprint model.

4.5.1 Footprint for Scintillometer Measurements

In general, footprint models determine the source area for measurements carried out at a single point in space. However, the scintillometer is a line measurement which requires a superposition technique in order to estimate the transfer function of a measurement.

The superposition is based in a discretization of the transect as a series of points where the measurement height for a point located at x', in the normalized path ($x' \in [0, 1]$), is given by the scintillometer beam height $Z(x')$. Then, the footprint of this point, for the atmospheric conditions, will be weighted by the normalized LAS weighting function, $G(x')$, in order to take into account the different contribution (bell-shaped) of each point along the path to the total LAS signal (see Eqs. (2.3) and (4.3)).

The procedure can be summarized by the following expression

$$f_{3D-LAS}(x, y) = \sum_{i=1}^{N} G(u_i) \cdot f_{3D}(x, y, Z(u_i)) \tag{4.15}$$

where the path is discretized into N points of location u_i, $i = 1, 2, ..., N$.

Fig. 4.4 shows the footprint calculated for the Valles Caldera National Preserve transect of the NM-LASNet (with a transect length of 2003 m) with wind direction perpendicular and parallel to the path. At the bottom is the footprint for an imaginary EC station located at the center of the transect and measuring at 3 m height. The top figures are the footprint estimated for the current transect ((a) parallel wind direction and (b) perpendicular wind direction). The domain for both maps is the same, showing qualitatively the large

difference between the footprint of the LAS and the EC, which is potentially useful for catchment scale studies, depending on the catchment size, and remote sensing algorithms validation and calibration. Also, from the quantitative point of view, the area that represents 95% of the footprint is 2.3 km^2 (perpendicular wind direction) and 1.3 km^2 (parallel wind direction) for the LAS and 0.09 km^2 for the EC, which is a difference of three orders of magnitude.

Meijninger et al. (2002) presents an interesting exercise to demonstrate the close relationship between the total size and position of the footprint and the wind direction and path orientation. When the wind blows perpendicular to the path, a broad transfer function is obtained, with the width mostly dependent on the path length. On the other hand, if the wind is blows parallel to the transect, the width of the footprint is much smaller and mostly dependent on the standard deviation of the crosswind component, but still considerably larger than a typical EC footprint.

In order to show that during changes in wind direction, the footprint of the LAS is more stable and better constrain than the footprint of the EC, a series of simulations were done for a fictitious LAS ($Z_eff = 10$ m and $L = 2000$ m) and EC ($Z = 10$ m). The atmospheric conditions were defined by $\sigma_v = 1$ m/s and $L_{MO} = -50$ m.

Fig. 4.5 shows the simulations for the LAS. The wind direction affects the size of the footprint, but the larger values remain in the same area, almost independent on the wind direction. This is advantageous, because the LAS is basically measuring average fluxes around the same area for all the simulated scenarios. On the other hand, Fig. 4.6 shows the same simulations for an EC

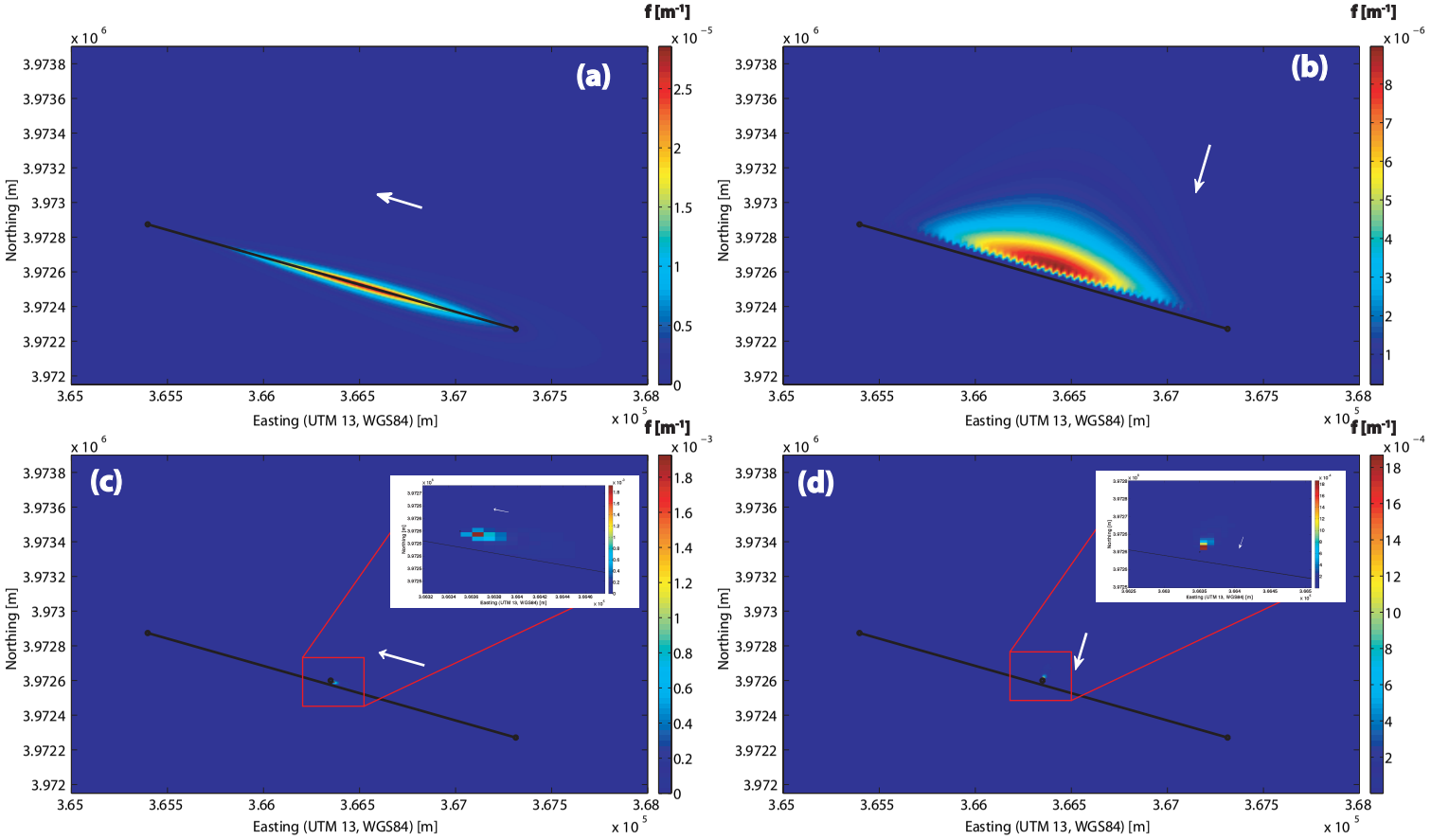

Figure 4.4: Footprint function $[m^{-1}]$ at the VCNP site on May 1, 2007 1400h MST for: (a) LAS with wind direction parallel to the transect (95% of the footprint function is represented by an area of 1.3 km^2), (b) LAS with wind direction perpendicular to the transect (95% of the footprint function is represented by an area of 2.3 km^2), (c) fictitious EC at 3 m height with wind direction parallel to the transect (95% of the footprint function is represented by an area of 0.09 km^2), (d) fictitious EC at 3 m height with wind direction perpendicular to the transect (95% of the footprint function is represented by an area of 0.09 km^2). Parameters used are: $\overline{U} = 5.5ms^{-1}$, $\overline{\theta} = 17.5$ degrees, $\sigma_\theta = 15.6$ degrees, $z_0 = 0.02m$, and $L_{MO} = -20$. The LAS transect was discretized in 50 points.

system. The footprint follows the wind direction, and given its small size, it will be highly affected by heterogeneities at this scale.

Finally, Fig. 4.7 compares the footprint's peak variability for both instruments. In this figure is evident that the fluxes measured by the LAS remain in the same area all the time, but the EC is measuring fluxes from different source areas depending on the wind direction.

4.5.2 Limitations of Footprint Models and its Use for Validation and Calibration of Remote Sensing Algorithms

Footprint estimation and validation of existing footprint models is still an open question in micrometeorology. With the increase of our measurement capabilities and infrastructure during the last decade, there is an interest in the scientific community to comprehend the representativeness of micrometeorological measurements. However it is not an easy task, due to the complexity of the problem. This complexity is evident when we take into account that (Foken and Leclerc, 2004): (i) the individual sources and sinks within the footprint are highly variable in time and space, (ii) the landscapes containing natural surfaces are intrinsically inhomogeneous in their bio-geochemical source properties, (iii) the vegetation has a specific response to environmental variables such as water stress, local cloud formation and sun angle, (iv) the gaseous exchange is species-dependent, (v) the properties up-wind and wind direction lead to considerable within-footprint spatial variability, (vi) the non-local advection is not easily separated from the within-footprint surface-atmosphere turbulent exchange data.

A few validation experiments of the models for fetch region estima-

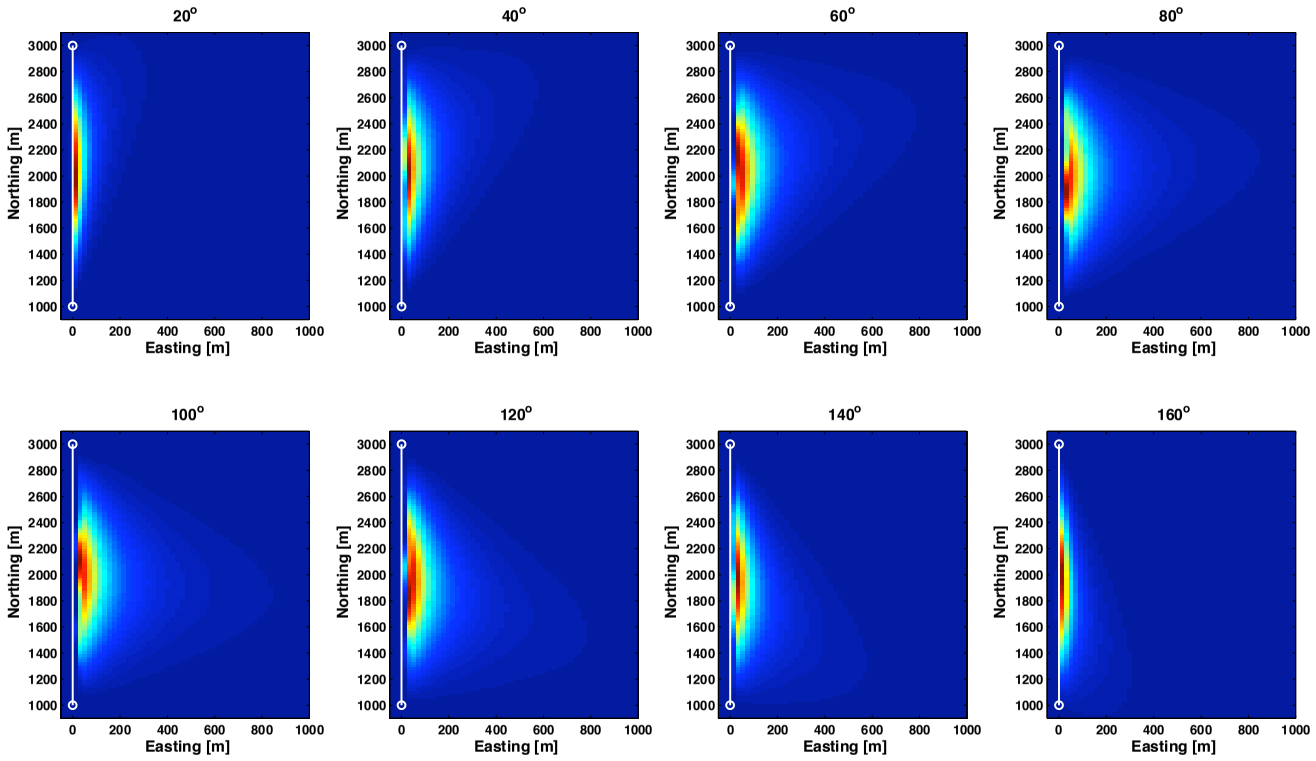

Figure 4.5: Variability of the footprint function with respect to the wind direction (azimuth) for a LAS. The color scale is not included, but the footprint values vary from high (red) to low (blue). The white line corresponds to the LAS transect. For the simulations: $L = 2000$ m, $\sigma_v = 1$ m/s, $L_{MO} = -50$ m, and $Z_eff = 10$ m.

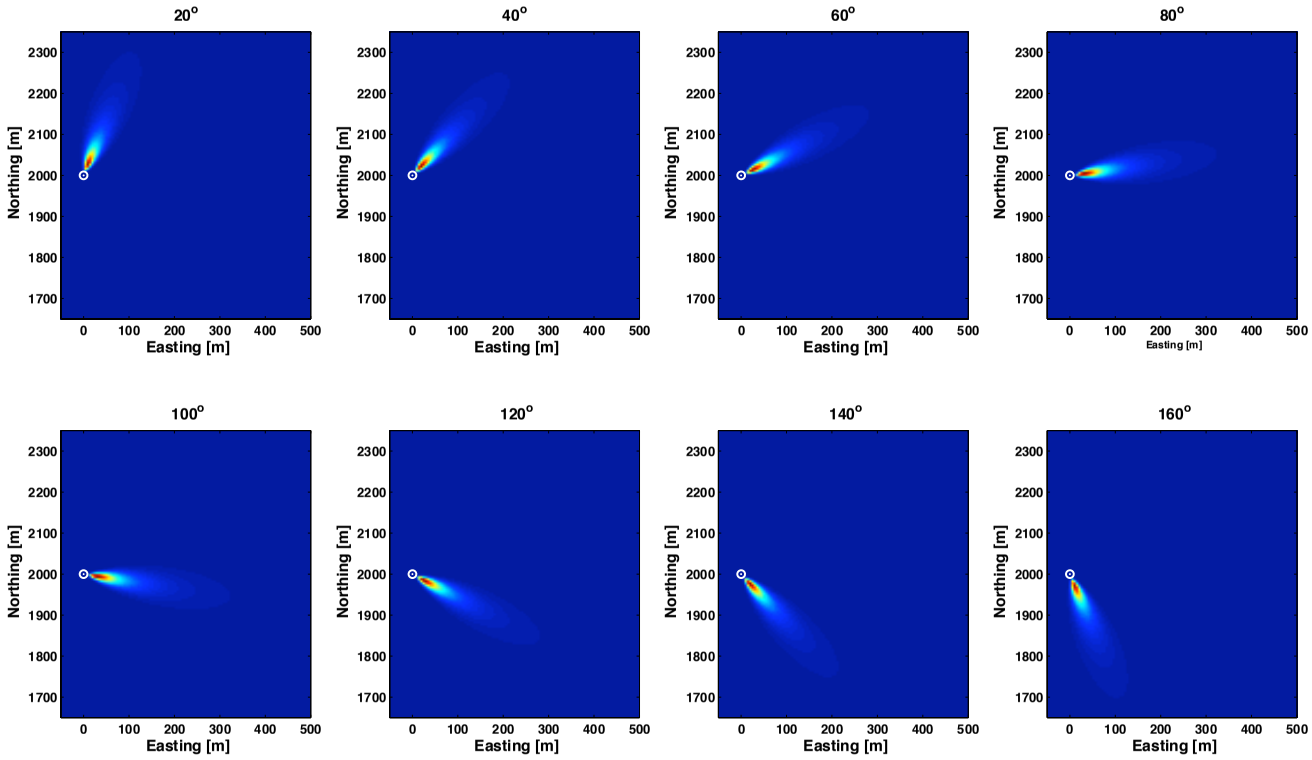

Figure 4.6: Variability of the footprint function with respect to the wind direction (azimuth) for a EC. The color scale is not included, but the footprint values vary from high (red) to low (blue). The white line corresponds to the LAS transect (Fig. 4.5). For the simulations: $\sigma_v = 1$ m/s, $L_{MO} = -50$ m, and $Z = 10$ m.

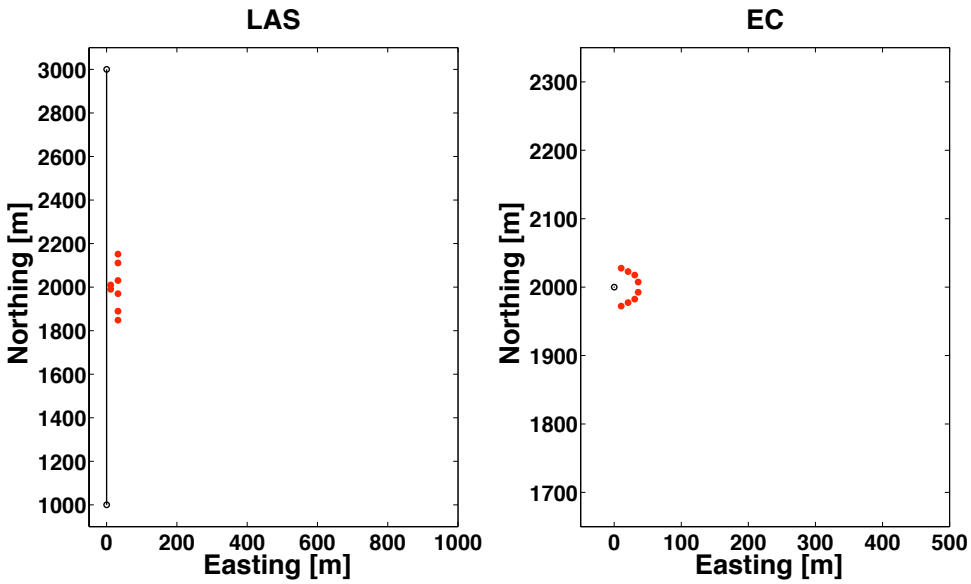

Figure 4.7: Variability of the footprint function with respect to the wind direction (azimuth) for an EC (Fig. 4.6) and LAS (Fig. 4.5). The red dots correspond to the peaks of the footprint for the wind direction used in Figs. 4.5 and 4.6. The black line corresponds to the LAS transect and the black circle to the EC. For the simulations: $\sigma_v = 1$ m/s, $L_{MO} = -50$ m, and $Z = 10$ m.

tion have been conducted (Marcolla and Cescatti, 2005; Göckede et al., 2005; Cooper et al., 2003; Finn et al., 1996; Leclerc et al., 1997, 2003a,b) and, to our knowledge, there are no detailed experiments addressing this question for the particular case of LAS. There are three common methods to validate these algorithms: (i) the use of artificial tracer gases such as sulfur hexafluoride (SF_6) (Leclerc et al., 2003a) or CO_2 (Leclerc et al., 1988), (ii) the use of natural sources of scalars such as water vapor (Cooper et al., 2003), CO_2 (Rannik et al., 2000) or sensible heat (Göckede et al., 2005), and (iii) the use of Large Eddy Simulation (LES) (Leclerc et al., 1997). Even though LES is a model, it can describe with great detail some simple situations, and therefore serve as a validation tool.

The validation and calibration of remote sensing algorithms with flux measurements on the ground is very sensitive on the footprint estimation. Hong et al. (2008) proposed to use a weighting factor for each pixel W_i within the footprint area to calculate an equivalent flux value from the derived image (latent or sensible heat flux). The weighting factor, which is valid for a scintillometer or EC, is shown in Eq. (4.16). Also, the equivalent fluxes are expressed in Eqs. (4.17) and (4.18), where H_i and λET_i are the pixel-scale H and λET estimated from the remote sensing algorithm.

$$W_i = \frac{f_{3D}(x, y, z_m)_i}{\sum_{j=1}^{N} f_{3D}(x, y, z_m)_j} \tag{4.16}$$

$$H_{FP} = \sum_{j=1}^{N} (W_i H_i) \tag{4.17}$$

$$\lambda ET_{FP} = \sum_{j=1}^{N} (W_i \lambda ET_i) \tag{4.18}$$

Two of the main problems with this approach are the presence of mixed pixels (just part of the pixel is within the footprint), especially for coarse resolution images (MODIS or GOES satellites) and the estimation of a representative daily footprint for a comparison with daily estimates of H and λET at daily scales, since the fetch is highly variable during the day. Obviously, footprint estimation and adequate comparison techniques play an important role in ground-truthing with the LAS and EC.

4.6 Effects of High Wind Speeds and Tower Vibrations

Fig. 4.8 shows sensible heat fluxes and net radiation measured in the Sevilleta National Wildlife Refuge during the intercomparison study done by Kleissl et al. (2008) on December 7, 2005. Four LAS and one EC system, located at the center of the transects, are compared during this windy day (see Fig. 4.8). The LAS overestimates H, measuring values even higher than the available energy, R_n, during unstable conditions before noon and during stable conditions at night. It is important to notice that the Obukhov length (L_{MO}) was around 1400 m during the evening of 12/7 when the large differences in H_{EC} and H_{LAS} were observed. This indicates near neutral conditions.

We suspect, given the high wind speeds, that the overestimation could be explained by two reasons (i) blowing dust causes differences in beam absorption and scattering, which is interpreted as variance increase in the signal strength and (ii) tripod vibrations are confused with intensity fluctuations.

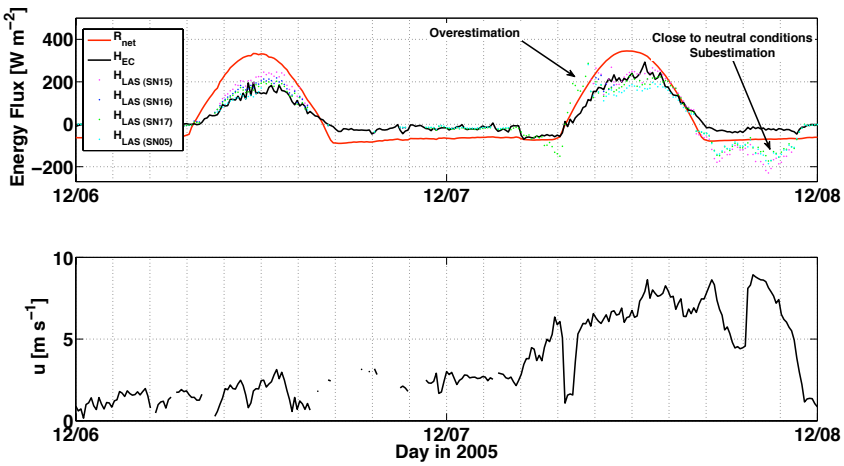

Figure 4.8: Top: Intercomparison of sensible heat flux measurements from four LASs (symbols), EC (purple line), and net radiation (black line) at the Sevilleta National Wildlife Refuge (SNWR) site (table 3.1) in December 7-8, 2005. Bottom: Wind speed at SNWR for the same days.

The second case could be tested and corrected, if high frequency data were stored, since this behavior can be observed in the demod power spectrum (Von Randow et al., 2008).

A method to correct the scintillometer signals for the effect of tower vibration was proposed by Von Randow et al. (2008). This approach compares the estimated Fourier spectra of the intensity fluctuations at the receiver and an expected theoretical shape of the spectrum (Clifford, 1971; Nieveen et al., 1998). Large deviations at frequencies between 1 and 10 Hz are attributed to tower vibrations and at higher frequencies, the differences are assumed to be caused by absorption. The correction of vibrations deserves more research, since they may occur in a broader range of frequencies.

4.7 Effects of Misalignment

The alignment procedure is a key issue in the accuracy of the LAS measurements. After the initial alignment, during set-up, special attention to the signal strength (demod) evolution may avoid overestimations of H due to misalignment. Fig. 4.9 shows a comparison of the sensible heat fluxes obtained from an EC and a LAS in SNWR, and the time evolution of the signal strength, which after the initial alignment (June 15) oscillates around a mean value of -110 mV, however, after June 25 a increasing trend in the demod value evidences the misalignment of the LAS. The Kipp & Zonen manual suggests to not use data with values of the signal strength (demod) higher than -50 mV.

The misalignment may be caused by tower vibrations due to high wind speeds, tectonic activity on the set-up site, or animal intervention. In this case, Fig. 4.10 shows the comparison between the period with good alignment (June 15-25, $H_{LAS} = 1.16H_{EC} + 48.5$ $[Wm^{-2}]$) and the period with misalignment (July 14-24, $H_{LAS} = 1.27H_{EC} + 81.7$ $[Wm^{-2}]$), that demonstrates how misalignment can increase the measured sensible heat flux.

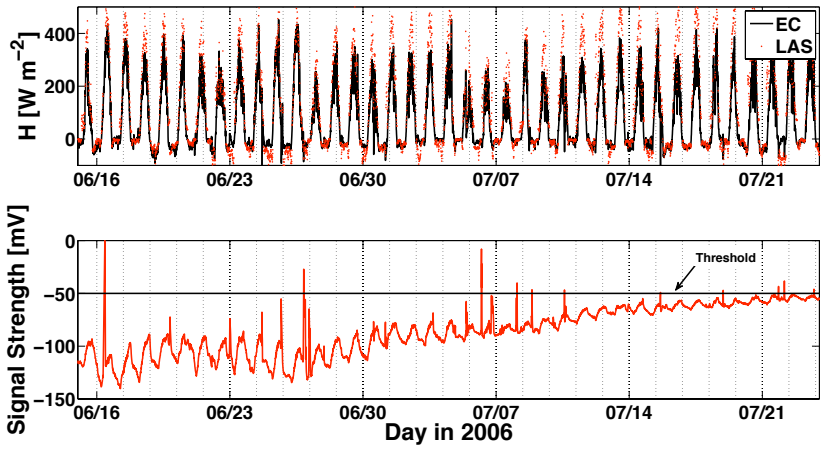

Figure 4.9: Top: Comparison of sensible heat fluxes estimated at SNWR during June-July of 2006 (EC black line and LAS red dots). Bottom: signal strength (demod) for the LAS.

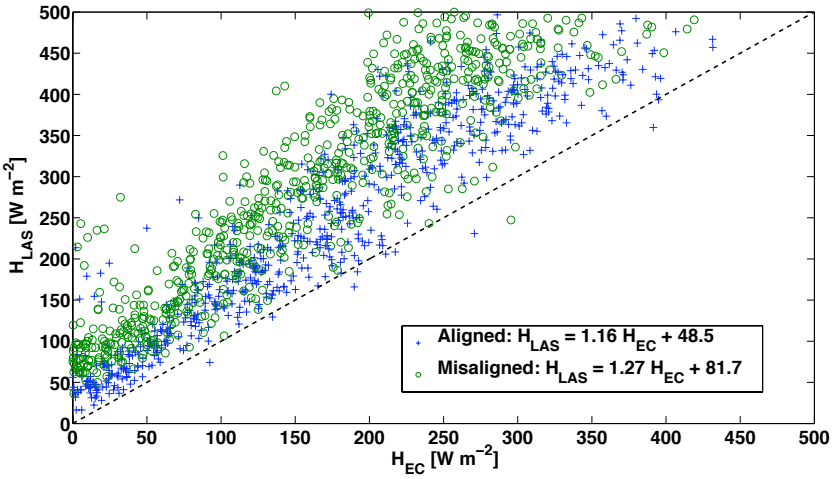

Figure 4.10: Scatter plot of sensible heat fluxes measured with a LAS and an EC system at SNWR during June-July of 2006.

CHAPTER 5

APPLICATIONS

5.1 Estimation of Sensible Heat Fluxes from LAS

Figs. 5.1 and 5.2 show the periods with data availability (red line) and the daily average sensible heat fluxes (H^{24}) for each NM-LASNet site, respectively. There are long periods of time with missing data, mainly due to power outages. The discontinuity in data do not reflect lack of robustness of the measurement system, but are caused by the difficult logistics of manpower and time to run, in a continuous fashion, a network of LASs spread over an area of 315,110 km^2 with limited cellular coverage for data transmission. The access to the sites, especially during winter, and the availability of students played a major role.

In order to estimate the average sensible heat flux over the day (H^{24}), an integration scheme following the trapezoidal integration method was used, i.e.,

$$H^{\tau} = \frac{\left(\int_0^{\tau} H(t)dt \right)}{\tau} \approx \frac{\left(\sum_{k=1}^{n} \frac{1}{2}(t_{k+1} - t_{k-1})H(t_k) \right)}{\tau} \tag{5.1}$$

where $H(t)$ is the variable of interest at time t, τ is the averaging period (24 hours in this case), and n is the number of data values during a particular day.

Fig. 5.2 shows that the higher daily sensible heat fluxes are in SNWR with an average value of 100 Wm^{-2} during the year and high values (approximately 200 Wm^{-2}) around July of 2006 and August of 2007. SAA, SAR, and VCNP have average H^{24} values of 25, 50, and 25 Wm^{-2} during the year, respectively.

However, for this data set, a consistent annual characterization of H is not possible (inter-annual variability) due to the short measurement period. Then, in order to characterize the fluxes at each site, an average diurnal cycle analysis was done for three particular periods (see Fig. 5.3): (i) Spring, (ii) Fall, and (iii) Winter. These intervals were chosen based on data availability and are expected to be good proxies for the typical behavior during each season.

Fig. 5.3 shows the average diurnal cycle analysis for (from left to right) Spring, Fall and Winter. The mean, standard deviation, and coefficient of variance were calculated for each hour as:

$$H = \frac{1}{n}\sum_{k=1}^{n} H_k \tag{5.2}$$

$$\sigma_H = \left[\frac{1}{n-1}\sum_{k=1}^{n}(H_k - H)^2\right]^{1/2} \tag{5.3}$$

$$CV_H = \frac{\sigma_H}{H} \tag{5.4}$$

where n is the number of elements of the sample.

In general, the sensible heat fluxes, during unstable conditions, tend to be higher in the places with more energy availability (R_n). From high to

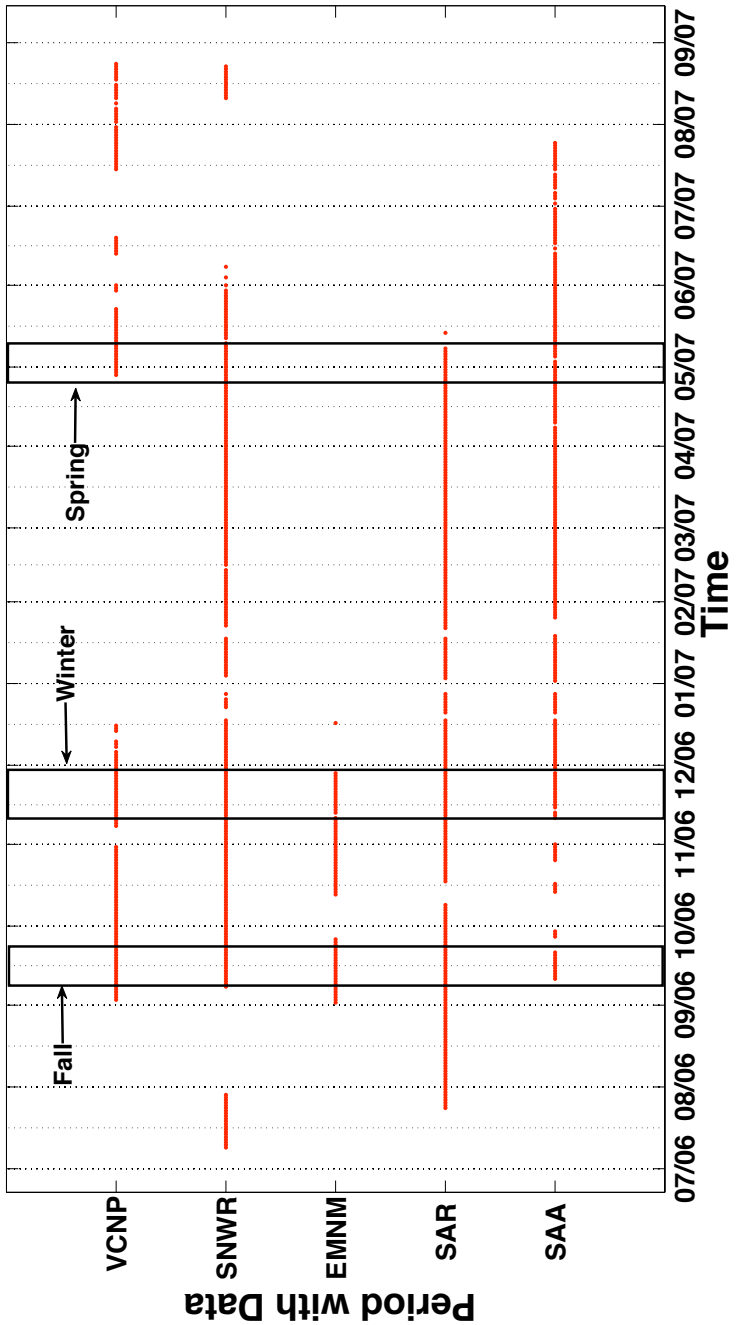

Figure 5.1: Periods with availability of sensible heat fluxes from the NM-LASNet. Three main time intervals were chosen for the diurnal cycle analysis: (i) Fall, (ii) Winter and (iii) Spring.

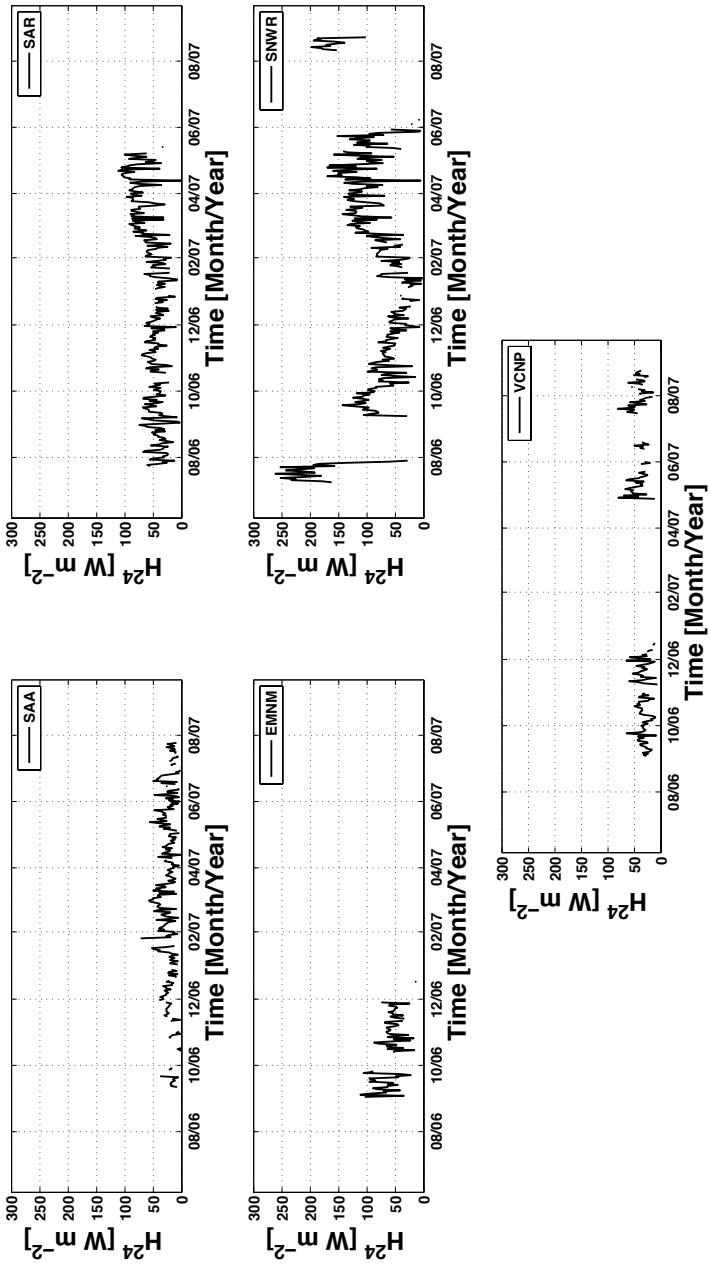

Figure 5.2: Daily sensible heat fluxes from the NM-LASNet.

low sensible heat fluxes the order is: SNWR, EMNM, SAR, VCNP, SAA. In an irrigated field, such as SAA, almost all the available energy for turbulent fluxes generation ($R_n - G$) is used for evapotranspiration. However, during the winter, the irrigation is shut off and evapotranspiration is limited by water availability leading to an small increase in H. At SAA, H is slightly higher in winter.

For the other sites, the maximum values of H are during the Spring, and decrease during Fall and Winter. Particularly, sensible heat fluxes in VCNP are close to SAA and even lower during some hours in the winter.

The coefficient of variation (CV) is a measure of how much the sensible heat is varying respect to its mean value. Nevertheless, since H is usually very low under stable conditions, CV increases and loses its meaning. Under unstable conditions, this variability is almost constant for all the sites during Spring (~ 0.5) and Winter (~ 0.4), but its is quite different in Fall, where Valles Caldera presents the higher variability. Finally, the fact that all sites have a similar CV and almost constant during unstable conditions, allows a better comparison, since all sites are varying in a similar fashion during unstable conditions.

5.2 Estimation of Evapotranspiration from LAS and the Energy Balance

The aim of this calculation is to show the potential of LAS as a tool, not only for validation and calibration of remote sensing algorithms (recall that no direct comparison between remote sensing and LAS was done in the study), but also for the estimation of evapotranspiration at field scale. This approach

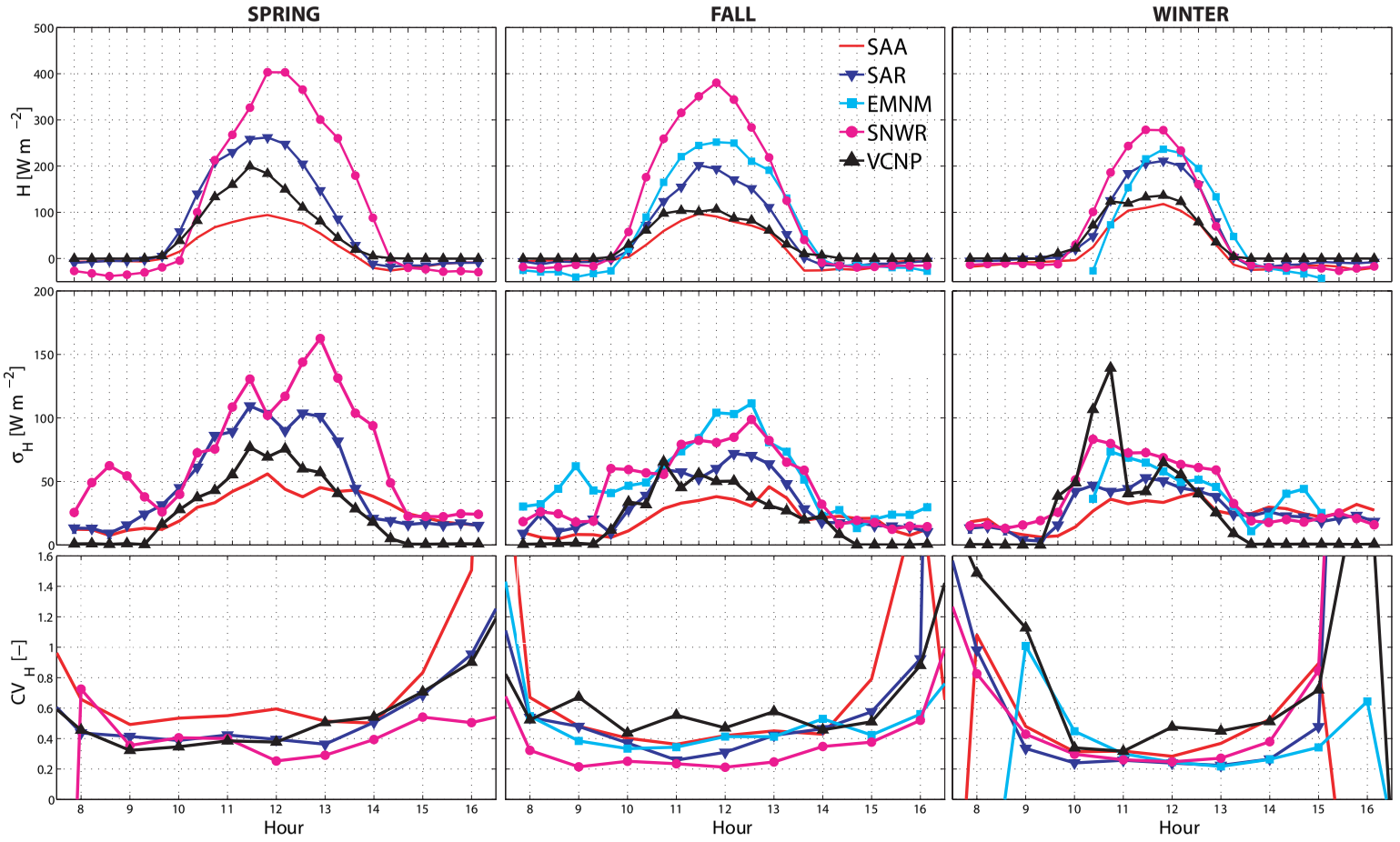

Figure 5.3: Average diurnal cycles at: SAA (red line), SAR (blue line with triangles), EMNM (blue line with squares), SNWR (purple line with circles), and , VCNP (black line with triangles). From upper row to bottom: Mean daytime evolution (H), standard deviation (σ_H), coefficient of variation ($CV = \frac{\sigma_H}{H}$), coefficient of variation during unstable atmospheric conditions ($CV = \frac{\sigma_H}{H}$). The Spring period is 04/2407 - 05/14/07, Fall is 09/07/06 - 09/24/06 and Winter is 11/07/06 - 12/01/06.

allows to acquire data in a continuous basis.

Latent heat fluxes (λET) are estimated as the residual of the surface energy balance (SEB) equation, at daily scales, using the sensible heat flux from the LAS, net radiation from a four component net radiometer, and soil heat flux from a flux plate and assuming SEB closure.

It is possible to write down an equation representing the inputs, losses, and storage of energy at the soil surface as (Campbell and Norman, 1998):

$$R_n - G = H + \lambda ET + S_p + S_c + S_s \tag{5.5}$$

where R_n represents the net radiation absorbed by the surface, G is the rate of heat loss to the deeper soil, H is the rate of loss of sensible heat flux, λET is the rate of loss of latent heat flux, S_p is the energy flux for photosynthesis, S_c is the canopy heat storage in biomass and water content, , S_s is the soil heat storage. However, in most cases non-local heat advection and heat storage within the vegetation layer and soil (S_p, S_c and S_s) are thought to be small and therefore ignored in the energy balance, simplifying Eq. (5.5)

$$R_n - G = H + \lambda ET \tag{5.6}$$

Eq. (5.6) is termed as the standard SEB equation. However, there are certain conditions under which the external advection of heat to the system plays an important role in the SEB. In areas where the air mass is strongly modified by arid conditions, the ratio $\lambda ET/R_n$ may be close to or even higher than 1 (De Bruin et al., 2005; Hoedjes et al., 2002). This may be the case in

irrigated areas surrounded by desert, such as the San Acacia Alfalfa site (SAA), that it is likely to have advection from Sevilleta, mainly during the early-mid growing season and premonsoon-period when the driest conditions are present in the region. However, no advection was observed with the LAS during the NM-LASNet measuring period.

The main problem with the advection of heat from up-wind sources (non-local advection) is that MOST not necessary applies. In the surface layer, when the non-local advection is of the same magnitude as the fluxes of one of the scalars generated by surface heating or evaporation, it appears that this scalar does not obey MOST (constant-flux layer does not exist), implying that T and q will behave in a non-similar fashion (De Bruin et al., 1999). Also, even if MOST applies, it is difficult to distinguish between local and non-local sensible heat measured by a LAS or EC, increasing the uncertainty in the footprint estimation. In the case of the scintillometer, the advection can be detected by the presence of a sudden drop in the structure parameter of the refraction index (C_n^2), during unstable conditions, which indicates a drop in H and a transition to stable conditions. Then the stable solution is used in the iterative process mentioned in section 2.1.1.

Theoretically, the SEB requires instantaneous closure, but it also can be written on a daily basis:

$$\lambda ET^{24} = R_n^{24} - G^{24} - H^{24} \tag{5.7}$$

where the superscript stands for an average flux over the 24-hour period (daily values). Then, in order to estimate the average components of the energy

balance over the day (R_n^{24}, H^{24}, G^{24}, λET^{24}), an integration scheme following the trapezoidal integration method was used, i.e.,

$$X^{\tau} = \frac{\left(\int_0^{\tau} X(t)dt \right)}{\tau} \approx \frac{\left(\sum_{k=1}^{n} \frac{1}{2}(t_{k+1} - t_{k-1})X(t_k) \right)}{\tau} \tag{5.8}$$

where $X(t)$ is the variable of interest at time t, τ is the averaging period (24 hours in this case), and n is the number of data values during a particular day.

A common assumption in Eq. (5.7) is that the ground heat flux is zero at daily scales ($G^{24} \approx 0$), then the average daily latent heat flux can be estimated as the difference between daily sensible heat flux and net radiation.

In the past, studies have been done with a similar approach, but with more data available for validation. Hoedjes et al. (2002) estimated latent heat fluxes under stable and unstable atmospheric conditions over an irrigated wheat field in a semi-arid region in northwest Mexico. They found that, using additional measurements of radiation, soil heat flux and wind speed, areally averages of both sensible and latent heat fluxes can be reliably predicted by LAS measurements, as long as the net radiation is greater than zero. Later, Hemakumara et al. (2003) used sensible heat from a LAS and net radiation to derive areally averaged actual evapotranspiration for a mixed vegetation area in Horana, Sri Lanka. Their results were compared with estimations obtained with the remote sensing based surface energy balance algorithm for land (SEBAL) (Bastiaanssen et al., 1998). The conclusion of this study was that for 10-days periods and monthly averages, the results from SEBAL and LAS

compared well. Furthermore, Hartogensis and De Bruin (2006) used optical scintillometry and net radiation measurements to estimate evapotranspiration at field-scales in an agricultural area in Idaho, during the RAPID experiment (De Bruin et al., 2005). They compared the LAS derived turbulent fluxes against the EC derived turbulent fluxes at 30 minute averages, with encouraging results. Finally, Schüttemeyer et al. (2006) examined the seasonal cycle of the components of the surface energy balance in the Volta basin in West Africa. They found good agreement between 30 minutes averages of sensible and latent heat fluxes from LAS and EC. Also, a direct comparison and the energy balance closure showed that both methods corresponded well during daytime, but during night time, the LAS seems to perform more realistically than the EC system.

Fig. 5.4 shows a comparison between the sensible heat fluxes measured with the LAS and the EC, for both sites. The regression slope is close to 1. However, the VCNP site presents higher random error, probably due to the distance between the EC and LAS set-ups.

Fig. 5.5 shows the daily values of the latent heat flux $[Wm^{-2}]$ and the other components of the SEB (to the right) and evapotranspiration $[mmday^{-1}]$ (to the left). In this figure, it is evident that the daily ground heat flux for the SNWR site can deviate from zero, while in the case of VCNP it is possible to assume $G^{24} \approx 0$.

The estimated values seem consistent, however it was not possible to validate them with the EC data or remote sensing products (e.g. $SEBAL^{NM}$). For VCNP, the increase in ET during June 10 may be explained by the rainfall

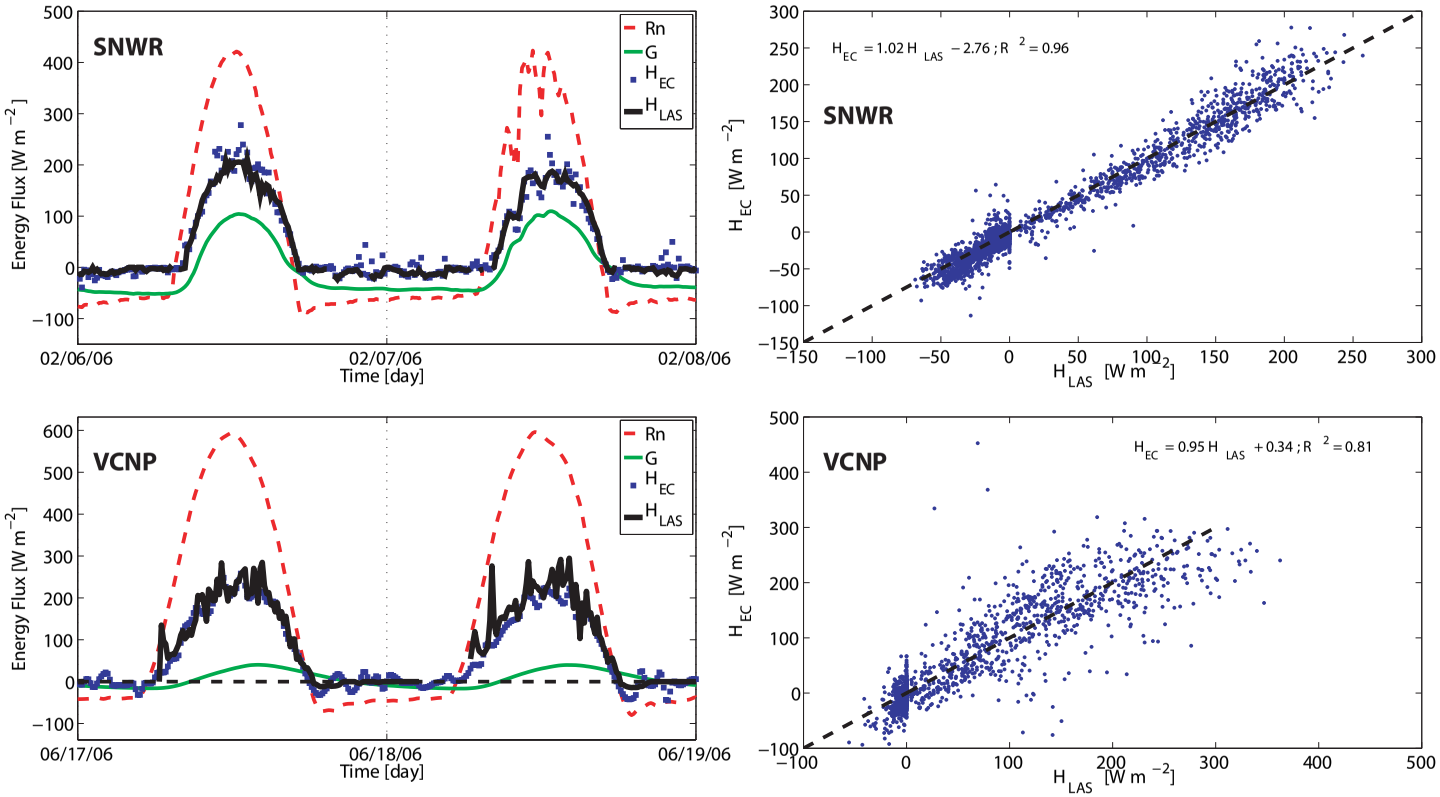

Figure 5.4: Data used for ET estimation: SNWR (upper row) and VCNP (lower row). In the figures to the left: R_n (red dashed line), G (green line), H_{LAS} (black line), and H_{EC} (blue squares). In the figures to the right: scatter plots of the sensible heat fluxes estimated with LAS (x-axis) and EC (y-axis).

events from June 6 to 9 (16 mm). On the other hand, for SNWR, the peak present on January 26 may be explained by the rainfall event on January 25 (approximately 1.3 mm), but the high value of ET on January 31 is an unknown. One possible explanation is a underestimation of the ground heat flux due to the lack of correction by storage.

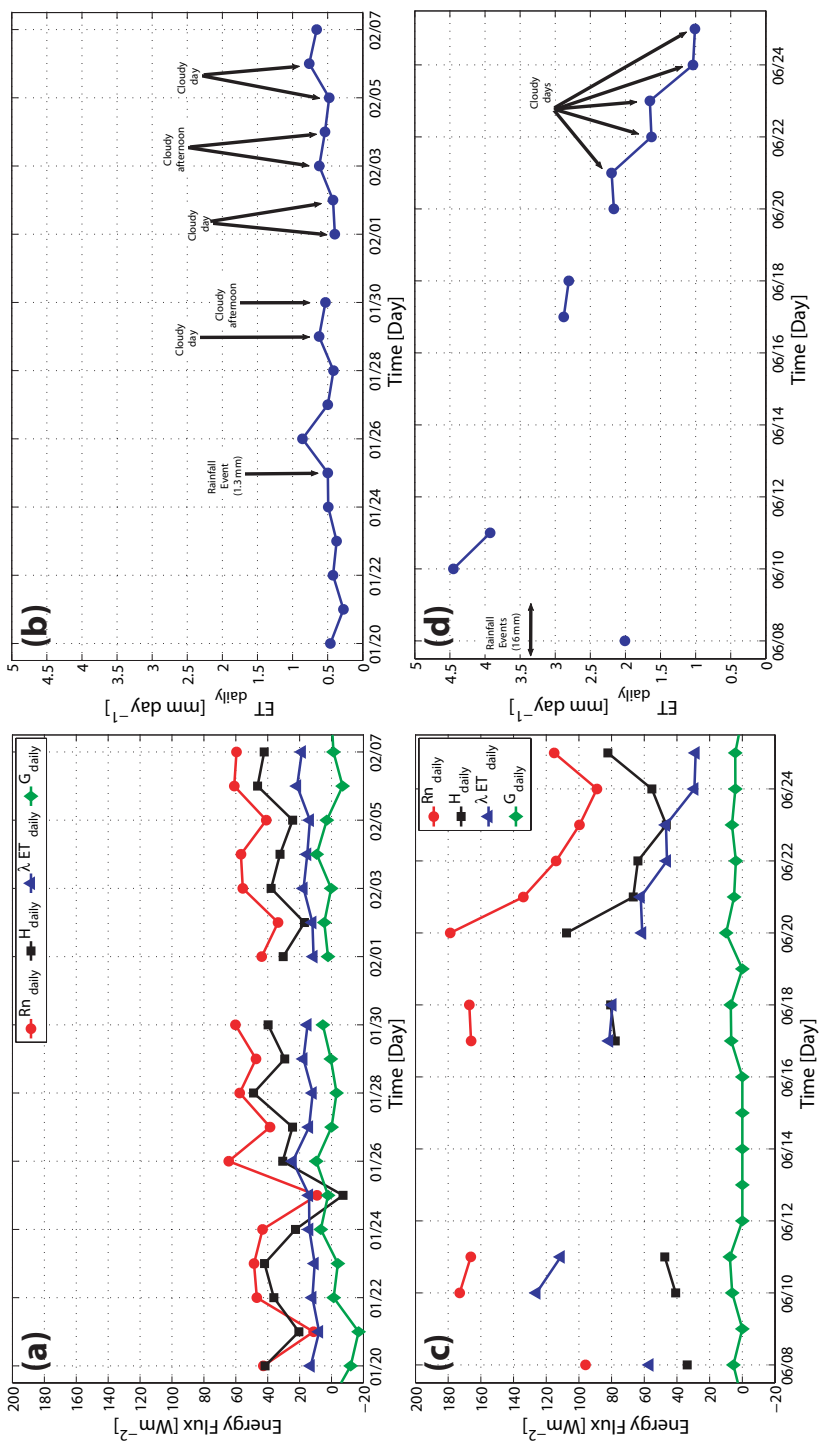

Figure 5.5: Daily latent heat flux for: (a)-(b) SNWR from January 20 to February 7 of 2006 and (c)-(d) VCNP from June 8 to June 25 of 2006 (lower row). In the figures to the left: R_n^{24} (red line with circles), H^{24} (black line with squares), G^{24} (green line with dots), and λET^{24} (blue line with triangles).

CHAPTER 6

GENERAL CONCLUSIONS AND LESSONS LEARNED

The main purpose of this thesis is to summarize the work done during the NM-LASNet set-up and related experiments, pointing out the most relevant experiences to date for evaluation and improvement of our operational procedures on scintillometry, particularly from a hydrological perspective. In addition, it is the aim of this research to share our lessons learned with colleagues who have an interest to employ the novel technology of scintillometry.

The installation of the New Mexico scintillometer network started in the fall of 2005 and was completed in September 2006. Thus, at this moment, there is an important data set of sensible heat flux measurements at each of the scintillometer transects under a wide range of weather conditions. Also, two experiments were done before and during the NM-LASNet operation. One is the intercomparison experiment, which was done with the instruments used on the network and focused on quantification of LAS accuracy. The second one focused on the study of saturation under strong turbulent conditions.

The scintillometer intercomparison experiments at the Sevilleta and in the Valles Caldera demonstrated that sensible heat fluxes measured by different scintillometers have an accuracy of $\pm 9\%$ or better (Kleissl et al., 2008). Some minor deviations are expected since it is not possible to set up two or

more scintillometer transects along exactly the same laser beam path since that would cause interference among the different instruments. This study was not described in detail in this thesis, but makes part of the related experiments and is well documented by Kleissl et al. (2008). The data collected during the saturation experiment is being processed, and it will be part of a forthcoming publication dealing with the onset of saturation and correction procedures.

From our practical experience with LAS, we can attest to the fact that they are much simpler to operate than EC systems. LASs are robust instruments and require little maintenance. One site visit every few months is sufficient to service the instrument. Due to spatial averaging, LASs give reliable sensible heat fluxes over durations as short as 1-5 minutes (depending on the transect length). Since the operation of LAS systems is much simpler than that of EC techniques, they have the potential to become common meteorological and hydrologic instruments, with a broad range of applications in agriculture, water management, meteorology, and hydrology, such as the validation and calibration of remote sensing algorithms for the estimation of evapotranspiration and hydrologic models. Future research may explore the usability of LAS measurements as data input for real time assimilation in hydrologic models, which, in principle, could improve the coupling with atmospheric circulations models.

Although the LAS is a robust technique, several technical issues have to be taken into account. The length of a scintillometer transect strongly depends on the height of the laser beam above the soil surface and the expected maximum sensible heat flux. The commonly reported maximum transect length

of 5000 m for a LAS is overly optimistic. For New Mexico conditions with maximum sensible heat fluxes exceeding 400 Wm^{-2}, a maximum transect length of 3000 m is more realistic if the beam height can be maintained at 30 m; for beam height 10 m the maximum transect length is about 1700 m. These transect lengths result in footprint areas which are not significantly larger than MODIS thermal pixels (one to three). In heterogeneous environments, this makes a comparison of LAS and satellite measurements difficult. Downscaling MODIS 1000x1000 m thermal pixels using 250x250 m visible and near-infrared pixels may be required, but this kind of approach will require a deeper understanding of the underlying processes behind the turbulent transport of energy fluxes and its behavior at different scales (Hong, 2008).

All the NM-LASNet scintillometers are powered by batteries that are charged by solar panels. Under ideal conditions of high insolation (SNWR and SAR transects), this setup works fine. However, where the solar panels are in the shade of hills (SAA and EMNM transects) or trees, or are covered with snow during the winter season (VCNP transect) power problems will cause loss of data. Special attention should be paid to install an adequate power supply.

LAS are easy to maintain but do require regular inspection of the signal strength that may weaken due to slow misalignment between emitter and receiver. When temporary towers are used for scintillometer support, we have found alignment problems to occur after heavy rainfall when the moist soil gives way causing the tower to settle. Misalignment increases the sensitivity of the measurements to tower vibrations and can thus introduce additional variance in the signal strength and overprediction of sensible heat fluxes. The

best way to prevent unnecessary field visits is to use wireless connections to the dataloggers that allow continuous real time inspection of the scintillometers. In our network, we successfully used 802.11 wireless radio (SNWR and SAR) and cellular (SAA) connections.

Several theoretical aspects have to be taken into account in order to obtain accurate measurements. In practical applications it is really hard to have an ideal set-up, because the location of the scintillometer is usually dictated by topographic restrictions and the necesity of large beam heights to avoid the effect of non-mixed internal boundary layers and saturation. Then, after the LAS is installed, a careful correction for non-ideal conditions has to be conducted, or at least taken into account as a source of uncertainty into the data. Particularly, the effective beam height has to be estimated as accurate as possible, especially over sloping terrain. The effect of external forcings, such as non-local and local advection has to be detected and quantified in order to be consistent in the choice of unstable or stable solutions for the sensible heat flux estimation and for the footprint estimation.

The footprint associated to the LAS measurements is typically three orders of magnitude larger and more stable that the EC footprint. This, allows to consider a broader range of scales and therefore more models for validation, calibration, and input of data for assimilation. Consistently, the scales of the footprint, for standard measurement techniques of the components of the SEB, are different, leading to an area-point comparison problem, when scintillometry is used for ET estimation. In the case of a soil heat flux plate, it is on the order of centimeters ($10^{-2}m^2$), for a net radiometer, it depends on the set-up height,

but in general it is a few square meters ($10m^2$), and for the LAS it is on the order of several square kilometers (10^7m^2). Then, there are still inconsistencies when areally averaged latent heat fluxes are derived from areally averaged measurements together with point measurements, especially with soil heat flux which posses a higher spatial variability. Future research has to be oriented to estimate R_n and G at larger scales, potentially from remote sensing data.

Moreover, the footprint of micrometeorological measurements is still an open question. The complexity of the processes and interactions involved in the transport of turbulent fluxes, makes this a difficult research field. The scientific community has dedicated much efforts on footprint research, but there is still considerable uncertainty associated to the fetch estimation. This fact adds uncertainty to the use of micrometeorological measurements for validation and calibration of remote sensing algorithms, since the footprint function cannot be accurately estimated. However, the current methods for the estimation of the footprint are useful, although subject to its restrictions and assumptions. The use of analytical models, such as the HKC-model, is a powerful approach, especially for operational applications.

Following the same idea, the use of LAS sensible heat flux measurements at the pixel scale for validation and calibration of remote sensing algorithms is a challenging question. The SEBAL and METRIC predicted sensible heat fluxes are biased, since they take care of biases in determination of net radiations and soil heat flux. Other remote sensing algorithms may have similar issues. The development of procedures to optimally use scintillometer sensible heat flux measurements for validation of remote sensing algorithm requires

more research.

Finally, LAS is a powerful measuring instrument which allows the estimation of sensible heat fluxes at scales comparable with the pixel-size of satellite images or grid cells of hydrologic and meteorological models. Also, with additional measurements of net radiation and ground heat flux, evapotranspiration rates can be estimated in a robust and continuous basis for hydrologic applications.

APPENDIX A

LIST OF SYMBOLS

Symbol	Units (SI)	Description
Bo	$-$	Bowen ratio
C_n^2	$m^{-2/3}$	Structure parameter of the refractive index of air
C_p^2	$Pa^2m^{-2/3}$	Structure parameter of water vapor
Cp	$Jg^{-1}K^{-1}$	Specific heat capacity of air
C_q^2	$kg^2m^{-6}m^{-2/3}$	Structure parameter of water vapor
C_T^2	$K^2m^{-2/3}$	Structure parameter of temperature
C_{Tq}	$Kkgm^{-3}m^{-2/3}$	Structure parameter of the covariante temperature and humidity
d	m	Zero displacement height
D	$-$	Aperture diameter of LAS
η	$gm^{-2}s^{-1}$	Scalar flux measured by a turbulent flux sensor (e.g. H, λET, CO_2)
ET	mm	Evapotranspiration
λET	Wm^{-2}	Latent heat flux
f	m^{-1}	Footprint of a a turbulent flux sensor
$G(x')$	$-$	Standardized weighting function to describes the contribution of each point along the path to the total LAS signal
H	Wm^{-2}	Sensible heat flux
κ	$-$	von Karman constant
L	m	LAS path length
l_0	m	Inner scale of turbulence
L_0	m	Outer scale of turbulence
L_{MO}	m	Obukhov length
n	$-$	Refraction index of air
p	Pa	Atmospheric pressure
Q_η	$gm^{-2}s^{-1}$	Source strength or surface flux
n	$kgkg^{-1}$	Specific humidity
T	K	Temperature scale

θ_*	K	Air temperature
$\sigma^2_{\ln(I)}$	$-$	Variance of the logarithm of the intensity fluctuations for an electromagnetic wave propagating through the atmosphere
σ_y	$-$	Crosswind spread of the plume for lateral dispersion
σ_θ	rad	Standard deviation of the horizontal wind direction
$W(x')$	m^{-5}	Weighting function that describes the contribution of each point along the path to the total LAS signal
K	rad/m	Optical wavenumber
k	rad/m	Spatial wavenumber
λ	μm	Scintillometer wavelength
x'	$-$	Dimensionless coordinate along a propagation path of length L
$\phi_n(k)$	m^3	Three-dimensional spectrum of refractive index fluctuations for the atmosphere
Ψ_m	$-$	Integrated stability function (Businger-Dyer correction)
T_y	s	Lagrangian time scale for the lateral dispersion
u	ms^{-1}	Wind speed measured at height z_u
u_*	ms^{-1}	Friction velocity
x	m	Up-wind distance
y	m	Crosswind distance
z_0	m	Roughness length
z_m	m	Turbulent flux sensor height
z_s	m	Length scale for HKC-model
Z_{LAS}	m	LAS height
Z_{eff}	m	LAS effective beam height

Bibliography

Allen, R. G., Tasumi, R., Trezza, R., 2006. Satellite-based energy balance for mapping evapotranspiration with internalized calibration (METRIC) − Model. J. Irrig. and Drain. Engrg., 133 (4), 380–394.

Anderson, M. C., Norman, J. M., Mecikalski, J. R., Torn, R. D., Kustas, W. P., Basara, J. B., 2004. A multi-scale remote sensing model for disaggregating regional fluxes to micrometeorological scales. J. Hydrometeorol., 5 (2), 343–363.

Andreas, E. L., 1989. Two-wavelength method of measuring path-averaged turbulent surface heat fluxes. J. Atmos. Oceanic Technol. 6, 280–292.

Andreas, E., 1988. Estimating C_n^2 over snow and sea ice from meteorological data. J. Opt. Soc. Am., 5, 481–495.

Baldocchi, D. and et al., 2001. Fluxnet: a new tool to study the temporal and spatial variability of ecosystem-scale carbon dioxide, water vapor and energy flux densities. Bull. Am. Meteorol. Soc., 82, 2415–2434.

Bastiaanssen, W. G. M., Menenti, M., Feddes, R. A., Holtslag, A. A. M., 1998. A remote sensing surface energy balance algortithm for land (SEBAL). Part 1: Formulation. J. Hydrol., 212-213, 198–212.

Bonan, G., 2002. Ecological Climatology, concepts and applications, Cambridge, UK, pp 678.

Campbell, G. S., Norman, J. M., 1998. An Introduction to Environmental Biophysics. Second Ed. Springer. pp. 286.

Clifford, S. F., 1971. Temporal-frequency spectra for a spherical wave propagating through atmospheric turbulence. J. Opt. Soc. Am., 61 (10), 1285–1292.

Clifford, S., Ochs, G., Lawrence, R., 1974. Saturation of optical scintillation by strong turbulence. J. Opt. Soc. Am., 64, 148–154.

Cooper, D. I., Eichinger, W. E., Archuleta, J., Hipps, L., Kao, J., Leclerc, M. Y., Neale, C. M., Prueger, J. H., 2003. Spacial source-area analysis of three-dimensional moisture fields from lidar, eddy covariance, and a footprint model. Agric. For. Meteorol., 114, 213–234.

Culf, A. D., Foken, T., Gash, J. H. C., 2004. The energy balance closure problem. In Kabat et al.: Vegetation, water, humans and the climate. A new perspective on an interactive system, Springer, Berlin, Heidelberg, 159–166.

De Bruin, H.A.R., Kohsiek, W., van den Hurk, B. J. J. M., 1993. A verification of some methods to determine the fluxes of momentum, sensible heat, and water vapor using standard deviation and structure parameter of scalar meteorological quantities. Bound. -Layer Meteorol., 63, 231–257.

De Bruin, H. A. R., van den Hurk, B. J. J. M., Kroon, L. J. M., 1999. On the temperature-humidity correlation and similarity. Bound. -Layer Meteorol., 93, 453–468.

De Bruin, H. A. R., 2002. Introduction, renaissance of scintillometry. Bound.

-Layer Meteorol., 105, 1–4. and the papers of this special issue on scintillometry.

De Bruin, H. A. R., Hartogensis, O. K., Allen, R. G., Kramer, J. W. J. L., 2005. Regional Advection Perturbations in an Irrigated Desert (RAPID) experiment. Theor. Appl. Climatol., 80, 143–152.

Draxler, R. R., 1976. Determination of atmospheric diffusion parameters. Atmos. Environ., 10, 99–105.

Finn, D., Lamb, B., Leclerc, M. Y., Horst, T. W., 1996. Experimental evaluation of analytical and Lagrangian surface-layer flux footprint models. Bound. -Layer Meteorol., 80, 283–308.

Flesch, T. K., Wilson, J. D., Yee, E., 1995. Backward-time Lagrangian stochastic dispersion models and their application to estimate gaseous emissions. J. Appl. Meteorol., 34, 1320–1332.

Foken, T., Leclerc, M. Y., 2004. Methods and limitations in validation of footprint models. Agric. For. Meteorol., 127, 223–234.

Gash, J. H. C., 1986. A note on estimating the effect of a limited fetch on micrometeorological evaporation measurements. Bound -Layer Meteorol., 35, 409–414.

Göckede, M., Markkanen, T., Mauder, M., Arnold, K., Leps, J-P, Foken, T., 2005. Validation of footprint models using natural tracer measurements from a field experiment. Agric. For. Meteorol., 135, 314–325.

Goodrich et al., 2000. Seasonal estimates of riparian evapotranspiration using remote and in-situ measurements. Agric. For. Meteorol., 105 (1), 281–309.

Gryning, S. E., Holtslag, A. A. M., Irwin, J. S., Sivertsen, B., 1987. Applied dispersion modeling based on meteorological scaling parameters. Atmos. Environ., 21 (1), 79–89.

Hadfield, M.G., 1994. Passive scalar diffusion from surface sources in the convective boundary-layer. Bound -Layer Meteorol., 69, 417–448.

Hafeez, M., Andreini, M., Liebe, J., Friesen, J., Marx, A., van de Giesen, N., 2007. Hydrological parameterization through remote sensing in Volta Basin,West Africa. Intl. J. River Basin Management, 5(1), 49–56.

Hartogensis, O. K., Watts, C. J., Rodriguez, J. C., De Bruin, H. A. R., 2003. Derivation of an Effective Height for Scintillometers: La Poza Experiment in Northwest Mexico. J. Hydrometeorol., 4, 915–928.

Hartogensis, O. K., and De Bruin, H. A. R., 2006. Estimating surface fluxes in irrigated areas with scintillometers. Computational Methods in Water Resources XVI.

Hemakumara, H. M., Chandrapala, L., Moene, A. F., 2003. Evapotranspiration fluxes over mixed vegetation areas measured from large aperture scintillometer. Agric. Water Manage., 58, 109–122.

Heusinkveld, B. G., Jacobs, A. F. G., Holtslag, A. A. M., Berkowicz, S. M., 2004. Surface energy balance in an arid region: role of soil heat flux. Agric. For. Meteorol., 122, 21–37.

Hendrickx, J. M. H., Hong, S-h., 2005. Mapping sensible and latent heat fluxes in arid areas using optical imagery. Proc. International Society for Optical Engineering, SPIE 5811, 138–146.

Hendrickx, J. M. H., Kleissl, J., Gomez, J. D., Hong, S-h., Fabrega, J., Vega, D., Moreno, H. A., Ogden, F. L., 2007. Scintillometer Networks for Calibration and Validation of Energy Balance and Soil Moisture Remote Sensing Algorithms. Proc. International Society for Optical Engineering, SPIE 6565.

Hill, R. J., Clifford, S. F., Lawrence, R. S., 1980. Refractive-Index and Absorption Fluctuations in the Infrared Caused by Temperature, Humidity and Pressure Fluctuations. J. Opt. Soc. Amer., 70, 1192–1205.

Hill, R. J., 1997. Algorithms for Obtaining Atmospheric Surface-Layer Fluxes from Scintillation Measurements. J. Atmos. Oceanic Technol., 14, 456–467.

Hoedjes, J. C. B., Zuurbier, R. M., Watts, C. J., 2002. Large aperture scintillometer used over a homogeneous irrigated area, partially affected by regional advection. Bound. -Layer Meteorol., 105, 99–117.

Hong, S-h., 2008. Mapping regional distribution of energy balance components using optical remotely sensed imagery. Ph.D. Dissertation, New Mexico Institute of Mining and Technology, New Mexico, United States.

Hong, S-h., Kleissl, J., Hendrickx, J. M. H., Allen, R. G., Bastiaanssen, W. G. M., Scott, R. L., Steinwand, A. L., 2008. Evaluation of SEBAL for mapping energy balance fluxes in arid riparian areas using remotely sensed optical imagery. (unpublished).

Horst, T. W., Weil, J. C., 1992. Footprint Estimation for Scalar Flux Measurements in the Atmospheric Surface Layer. Bound. -Layer Meteorol., 59, 279–296.

Horst, T. W., Weil, J. C., 1994. How far is far enoughthe fetch requirements for micrometeorological measurement of surface fluxes. J. Atmos. Oceanic Technol., 11, 1018–1025.

Horst, T. W., 1999. The footprint for estimation of atmosphere-surface exchange fluxes by profile techniques. Bound. -Layer Meteorol., 90, 171–188.

Hsieh, C., Katul, G., Chi, T., 2000. An approximate analytical model for footprint estimation of scalar fluxes in thermally stratified atmospheric flows. Adv. Water Resour., 23, 765–772.

Katul, G. and et al., 1999. Spatial variability of turbulent fluxes in the roughness sublayer of an even-aged pine forest. Bound.-Layer Meteorol. 93, 1–28.

Kipp & Zonen, 2007. Instruction Manual: Large Aperture Scintillometer. Kipp & Zonen. pp. 74.

Kleissl, J., Gomez, J. D., Hong, S-h., Hendrickx, J. M. H., Rahn, T., Defoor, W., 2008. Large aperture scintillometer intercomparison study. Submitted to Bound. -Layer Meteorol.

Kljun, N., Rotach, M. W., Schmid, H. P., 2002. A 3-D backward Lagrangian footprint model for a wide range of boundary layer stratifications. Bound. -Layer Meteorol., 103, 205–226.

Kolmogorov, A. N., 1941. Local structure of turbulence in an incompressible liquid for ever large Reynolds numbers. Dokl. Akad. Nauk SSSR., 30(4), 299–303.

Kohsiek, W., Meijninger, W. M. L., Moene, A. F., Heusinkveld, B. G., Hartogensis, O. K., Hillen, W. C. A. M., De Bruin, H. A. R., 2002. An extra large aperture scintillometer for long range applications. Bound. -Layer Meteorol., 105, 119–127.

Kohsiek, W., Meijninger, W.M.L., De Bruin, H. A. R., Beyrich, F., 2006. Saturation of the Large Aperture Scintillometer. Bound. -Layer Meteorol., 121, 111–126.

Leclerc, M. Y., Shen, S. H., Lamb, B., 1997. Observations and large-eddy simulation modeling of footprints in the lower convective boundary layer. J. Geophys. Res. Atmos., 102, 9323–9334.

Leclerc, M. Y., Karipot, A., Prabha, T., Allwine, G., Lamb, B., Gholz, H. L., 2003a. Impact of non-local advection on flux footprints over a tall forest canopy: a tracer flux experiment (Special issue: Advances in micrometeorology: Tribute to G.W. Thurtell). Agric. For. Meteorol., 115, 17–34.

Leclerc, M. Y., Meskhidze, N., Finn, D., 2003b. Footprint predictions comparison with a tracer flux experiment over a homogeneous canopy of intermediate roughness. Agric. For. Meteorol., 117, 17–34.

Leclerc, M. Y., Thurtell, G. W., Kidd, G. E., 1988. Measurements and Langevin simulations of mean tracer concentration fields down-wind from a circular

line source inside and above an alfalfa canopy. Bound. -Layer Meteorol., 43, 287–308.

Mahrt, L., 1998. Flux sampling errors for aircraft and towers. J. Atmos. Oceanic Technol. 15, 416–429.

Marcolla, B., Cescatti, A., 2005. Experimental analysis of flux footprint for varying stability conditions in an alpine meadow. Agric. For. Meteorol., 135, 291–301.

Martano, P., 2000. Estimation of Surface Roughness Length and Displacement Height from Single-Level Sonic Anemometer Data. J. Appl. Meteorol., 39, 708–715.

Meijninger, W. M. L., De Bruin, H. A. R., 2000. The sensible heat flux over irrigated areas in western Turkey determined with a large aperture scintillometer. J. Hydrology. 229, 42–49.

Meijninger, W. M. L., Hartogensis, O. K., Kohsiek, W., Hoedjes, J. C. B., Zuurbier, R. M., De Bruin, H. A. R., 2002. Determination of area-averaged sensible heat fluxes with a large aperture scintillometer over a heterogeneous surface – Flevoland field experiment. Bound. -Layer Meteorol., 105, 37–62.

Meijninger, W. M. L., 2003. Surface fluxes over natural landscapes using scintillometry. Ph.D. Dissertation, Wageningen University, Wageningen, The Netherlands.

Middle Rio Grande Water Assembly, 1999. Middle Rio Grande water budget

(where water comes from, and goes, and how much): averages for 1972-1997. Middle Rio Grande Council of Governments of New Mexico. 10 pages.

Norman, J. M., Kustas, W. P., Humes, K. S., 1995. A two-source approach for estimating soil and vegetation energy fluxes from observations of directional radiometric surface temperature. Agric. For. Meteorol., 77, 163–293.

Nieveen, J. P., Green, A. E., Kohsiek, W., 1998. Using a large-aperture scintillometer to measure absorption and refractive index fluctuations. Bound. -Layer Meteorol., 87, 101–116

Ochs, G. R., Hill, R. J., 1982. A study of factors influencing the calibration of optical C2n meters. NOAA Tech. Memo. ERL WPL-232. NOAA Environmental Research Laboratory: Boulder, CO. p. 24.

Oke, T. R., 1987. Boundary layer climates. Routledge, 435 pp.

Panofsky, H., Dutton, J., 1984. Atmospheric Turbulence. John Wiley & Sons, New York.

Pasquill, F., 1972. Some aspects of boundary layer description. Quart. J. Roy. Meteorol. Soc., 98, 469–494.

Pasquill, F., Smith, F. B., 1983. Atmospheric diffusion. 3rd Edition. Wiley, New York, 437 pp.

Peters Lidard, C. D., Kumar, S. V., Tian, Y., Eastman, J. L., Houser, P., 2004. Global urban-scale land-atmosphere modeling with the land information system. 84th AMS Annual Meeting 11-15 January 2004, Symposium on Planning, Nowcasting, and Forecasting in the Urban Zone.

Rannik, Ü., Aubinet, M., Kurbanmuradov, O., Sabelfeld, K. K., Markkanen, T., Vesala, T., 2000. Footprint analysis for measure-ments over heterogeneous forest. Bound. -Layer Meteorol., 97, 137–166.

Reynolds, A. M., 1998. A two-dimensional Lagrangian stochastic dispersion model for convective boundary layers with wind shear. Bound. -Layer Meteorol., 86, 345–352.

Rodean, H., 1996. Stochastic Lagrangian models of turbulent diffusion. Meteorological Monographs, Vol. 26, No. 48. American Meteorological Society, Boston, pp. 84.

Rotach, M. W., Gryning, S. -E., Tassone, C., 1996. A two-dimensional stochastic dispersion model for daytime conditions. Quart. J. Roy. Meteorol. Soc., 122, 367–389.

Schellekens, J., Bruijnzeel, L. A., Scatena, F. N., Bink, N. J., Holwerda, F., 2000. Evaporation from a tropical rain forest, Luquillo Experimental Forest, Puerto Rico. Water Resour. Res., 36(8), 2183–2196.

Schmid, H. P., 2002. Footprint modeling for vegetation atmosphere exchange studies: a review and perspective. Agric. For. Meteorol., 113, 159–183.

Schmid, H. P., T. R., Oke. 1990. A model to estimation the source area contributing to turbulent exchange in the surface layer over patchy terrain. Q.J.R. Meteorol. Soc. 116, 965–988.

Schüttemeyer, D., Moene, A. F., Holtslag, A. A. M., De Bruin, H. A. R., Van

De Giesen, N., 2006. Surface fluxes and characteristics of drying semi-arid terrain in west Africa. Bound. -Layer Meteorol., 118, 583–612.

Stull, R. B., 1988. An introduction to boundary layer meteorology. Kluwer Academic Publishers. The Netherlands, pp 666.

Thomson, D. J., 1987. Criteria for the selection of stochastic models of particle trajectories in turbulent flow. J. Fluid Mech., 180, 529–556.

Van Dijk, A., Moene, A. F., De Bruin, H. A. R., 2004. The principles of surface flux physics: theory, practice and description of the ECPACK library, Internal Report 2004/1, Meteorology and Air Quality Group, Wageningen University, Wageningen, the Netherlands, 99 pp.

Von Randow, C., Kruijt, B., Holtslag, A. A. M., de Oliveira, M. B. L., 2008. Exploring eddy-covariance and large-aperture scintillometer measurements in an Amazonian rainforest. Agric. For. Meteorol., 148, 680–690. (In Press).

Wang, T-i., Ochs, G. R., Clifford, S. F., 1978. A saturation-resistant optical scintillometer to measure C_n^2. J. Opt. Soc. Am., 68 (3), 334–338.

Weber, R. O., 1998. Estimators for the standard deviations of lateral, longitudinal and vertical wind components. Atmos. Environ., 32 (21), 3639–3646.

Wilson, J. D., Sawford, B. L., 1996. Review of Lagrangian stochastic models for trajectories in the turbulent atmosphere. Bound. -Layer Meteorol., 78, 191–210.

Wilson, K. and et al., 2002. Energy balance closure at FLUXNET sites. Agric. For. Meteorol., 113, 223–243.

Wyngaard, J., Izumi, Y., Jr, S. C., 1971. Behavior of the refractive-index-structure parameter near the ground. J. Opt. Soc. Am., 61, 1646–1650.

Yamartino, R. J., 1984. A comparison of several śingle-passéstimators of the standard deviation of wind direction. J. Climate Appl. Meteorol., 23, 1362–1366.